Mechanical Systems and Signal Processing 234 (2025) 112790

Contents lists available at ScienceDirect

Mechanical Systems and Signal Processing

journal homepage: www.elsevier.com/locate/ymssp

Full Length Article

A methodology for analysing the influence of design variables in beams with eddy current damping

Mikel Brun [*], Fernando Cortés, María Jesús Elejabarrieta

Department of Mechanics, Design and Industrial Management, University of Deusto, Avda. de las Universidades 24, 48007 Bilbao, Spain

ARTICLE INFO

Communicated by J.C. Ji

Keywords:
Eddy currents
Vibrating beam
Motional induction
Design strategies
Parametric study
Finite difference method

ABSTRACT

Vibration attenuation is a critical aspect of mechanical engineering design, and eddy currents provide an effective damping technique that does not add mass to the system, and it is especially effective at low frequencies. In this context, this paper introduces a methodology tailored for the design of thin non-magnetic metallic beams with eddy current damping. By solving the eddy current problem for a reference beam across various boundary conditions and lengths, a comprehensive database of output variables is generated. These include structural and electrical variables, along with coefficients from two simplified equivalent beam models: an electromechanical model and a Kelvin-Voight viscoelastic model. Simplified equations are subsequently derived to predict the behaviour of other beams, eliminating the need to solve complex electromechanical problems individually. The methodology incorporates a parametric study of design variables, including beam geometry, material properties, velocity magnitude, magnetic field strength, and boundary conditions, revealing straightforward relationships between these variables and damping performance. Moreover, insights into eddy current maps are provided, emphasising their dependence on boundary conditions. This approach significantly streamlines the design process, enabling efficient and precise vibration attenuation. The methodology, further supported by a MATLAB application included as supplementary material, constitutes an invaluable resource for engineering design.

1. Introduction

Foucault currents, also known as eddy currents due to their swirling nature, are generated whenever an electric field is induced in a conducting medium [1]. This well-known phenomenon, first observed in 19-th century, has remained a consistent area of research due to the multitude of studies and applications that have emerged since its discovery. These studies aim either to mitigate the effects of induced eddy currents or to exploit them for beneficial purposes. Numerous mechanical applications have been developed around eddy currents, such as braking systems [2,3] and seismic control mechanisms [4,5], among many others.

In mechanical engineering, vibration attenuation is of paramount importance, and damping by induced eddy currents is one of the many passive damping techniques employed to achieve this in structural systems [6,7]. This method is particularly advantageous as it is effective at lower frequencies compared to more traditional damping techniques and, importantly, it does not add mass to the system, operates instantaneously, and possesses a reversible nature. Numerous studies have focused on eddy current damping. For

---

* Corresponding author.
E-mail addresses: mikel.brun@opendeusto.es (M. Brun), fernando.cortes@deusto.es (F. Cortés), maria.elejabarrieta@deusto.es (M.J. Elejabarrieta).

https://doi.org/10.1016/j.ymssp.2025.112790
Received 16 January 2025; Received in revised form 14 March 2025; Accepted 23 April 2025

instance, in [8], a negative stiffness eddy-current damper is proposed for cable vibration control. In [9], a novel magnetic spring-damper is designed, consisting of a conducting aluminium plate and two permanent magnets, where the dynamic damping characterisation employs the differential Buoc-Wen model. In [10], a negative stiffness eddy-current damper is proposed and validated numerically and experimentally for the vibration control of large-scale engineering structures. In [11], a tuned mass damper with eddy current damping is designed, consisting of two fixed conductive plates and eight rectangular permanent magnets, for structural vibration control. In [12], the eddy current damping forces in a moving conductor are enhanced by splitting the external magnetic field into multiple fields with alternating directions, generating multiple loops with reduced electrical resistance. Furthermore, combining other damping techniques with eddy current damping has proven to be highly efficient [13]. Of the various types of structural systems that have been studied in the literature, beams are among the most commonly utilised in numerous practical applications, such as in aircraft wings [14] or vehicle front ends [15]. However, studies specifically addressing the mitigation of vibrations by combining structural beams with eddy current dampers remain limited, as this area is still in the developmental phase [5]. These studies primarily focus on the practical implementation of eddy current dampers and their correlation with experimental data [16,17], rather than on a detailed examination of the nature of induced eddy currents and their effects on aspects such as damping forces and power dissipation, among others. As a thorough understanding of induced eddy currents is crucial for accurately predicting energy dissipation, extensive knowledge of their properties is essential for effective design aimed at maximising energy dissipation. A previous comprehensive study by the authors exists in which induced eddy currents were numerically analysed on a thin non-magnetic conducting metallic beam in the presence of a static and uniform magnetic field, considering different bending or torsional mode shapes [18].

Here, this paper aims to perform a comprehensive parametric study of the design variables influencing beams with eddy current damping, focusing on their dynamic and electrical characteristics and vibration attenuation capacity. The beam vibrates under an applied magnetic field, with bending mode shapes characterising the vibration. Small amplitudes of vibration are assumed throughout this work in order to approximate the system's behaviour as linear. The design variables considered include beam geometry (length, width, and thickness), material properties (Young's modulus, volumetric density, and electrical conductivity), bending velocity magnitude, magnetic field magnitude, and ten combinations of boundary conditions (free, clamped, sliding and pinned).

The physical system can be modelled using a single-degree-of-freedom electromechanical model, which, under the assumption of negligible self-inductance, is equivalent to a Kelvin-Voight mechanical model, as outlined in [19]. These models were validated both experimentally [20] and through direct comparison with numerical results provided in [21], and are therefore selected in this work to model the beam with eddy current damping. These models offer significant insights into the damping behaviour induced by eddy currents. As a result, the output variables for the first four bending modes include electrical variables (maximum current density, average dissipated power, and total current), structural variables (angular natural frequency and stiffness), as well as coefficients from the electromechanical model (electrical resistance and bar length) and the Kelvin-Voight mechanical model (viscous coefficient and viscous damping ratio).

The proposed methodology involves examining the equations of the output variables, revealing straightforward relationships between these variables and the design variables, except for the beam length and boundary conditions. Consequently, a reference beam is studied in detail for each of the ten boundary conditions by varying the ratio between the beam length and a fixed width. In these cases, the complete eddy current problem must be solved numerically. However, using the relationships established for the design variables and results for the reference beam, the methodology can be extended to design other beams without solving for the eddy currents directly. This significantly simplifies the design process, enabling designers to predict the behaviour of beams with eddy current damping using only their geometry and material properties, thereby eliminating the need for complex numerical procedures.

The structure of the article is as follows: after the introduction in Section 1, Section 2 presents the beam with eddy current damping under study and describes the design variables for analysis. Section 3 details the electromechanical model of the system introduced in Section 2 and its equivalent Kelvin-Voight mechanical model, including the respective coefficients of each model. Section 4 outlines the numerical procedure used to solve for the eddy currents in the reference beam and stablishes the output variables to be extracted. Section 5 provides a brief analysis of the nature of the induced eddy currents for two beam boundary conditions. Section 6 presents the parametric study and the design methodology, initially outlining the relationships identified between the output and design variables, followed by a study of the influence of the beam length for the ten different beam boundary conditions of the reference beam, and concluding with an example illustrating how the methodology can be generalised to predict results for any design beam. Additionally, Appendix provides eddy current density maps for the first four bending modes across all ten boundary conditions. Lastly, a MATLAB application is provided as supplementary material to assist designers in determining the attenuation introduced in any design beam with eddy current damping.

2. Description of the beam with eddy current damping

The beam with eddy current damping under study consists of a thin, metallic non-magnetic beam under one of the ten boundary conditions presented in Table 1. Fig. 1 illustrates the particular case of a free-free beam. The beam is subjected to an external magnetic field denoted by $\boldsymbol{B}_{\mathrm{e}}$, and undergoes a harmonic vibration represented by a velocity field with a spatial distribution given by $\boldsymbol{v}(x)$. Owing to the assumption of small vibration amplitudes and the application of Euler-Bernoulli beam theory, only velocity in the z-direction exists, such that $\boldsymbol{v}(x) = v(x)\widehat{\boldsymbol{z}}$, where $v(x)$ represents the spatial distribution. The interaction between the motion and the external magnetic field induces harmonic eddy currents, with their spatial distribution defined by the current density vector field $\boldsymbol{J}(x,y)$. Since the beam is thin, the currents are only induced in the x - y plane and thus, their spatial distribution can be expressed as

$$\boldsymbol{J}(x,y) = J_x(x,y)\widehat{\boldsymbol{x}} + J_y(x,y)\widehat{\boldsymbol{y}}, \tag{1}$$

Table 1
Modal characteristics for the ten different beam boundary conditions [22].

Case	$\widetilde{v}_r(x)$	Transcendental Equation for λ_r	κ_r	β_r	m_r
1. Free-Free 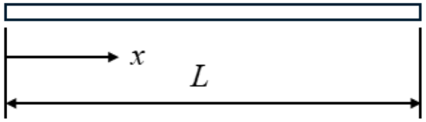	$\cosh\left(\frac{\lambda_r x}{L}\right)+\cos\left(\frac{\lambda_r x}{L}\right)$ $-\kappa_r\left(\sinh\left(\frac{\lambda_r x}{L}\right)+\sin\left(\frac{\lambda_r x}{L}\right)\right)$	$\cos\lambda_r\cosh\lambda_r - 1 = 0$	$\frac{\cosh\lambda_r-\cos\lambda_r}{\sinh\lambda_r-\sin\lambda_r}$	2, $\forall r$	$m/4$
2. Free-Sliding 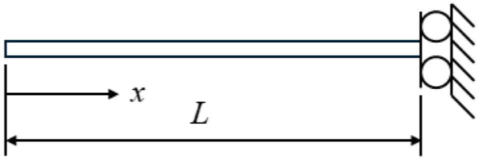	$\cosh\left(\frac{\lambda_r x}{L}\right)+\cos\left(\frac{\lambda_r x}{L}\right)$ $-\kappa_r\left(\sinh\left(\frac{\lambda_r x}{L}\right)+\sin\left(\frac{\lambda_r x}{L}\right)\right)$	$\tan\lambda_r + \tanh\lambda_r = 0$	$\frac{\sinh\lambda_r-\sin\lambda_r}{\cosh\lambda_r+\cos\lambda_r}$	2, $\forall r$	$m/4$
3. Clamped-Free 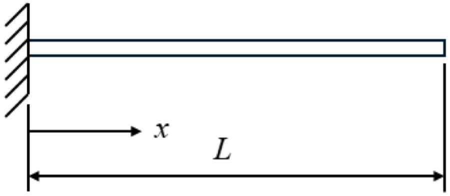	$\cosh\left(\frac{\lambda_r x}{L}\right)-\cos\left(\frac{\lambda_r x}{L}\right)$ $-\kappa_r\left(\sinh\left(\frac{\lambda_r x}{L}\right)-\sin\left(\frac{\lambda_r x}{L}\right)\right)$	$\cos\lambda_r\cosh\lambda_r + 1 = 0$	$\frac{\sinh\lambda_r-\sin\lambda_r}{\cosh\lambda_r+\cos\lambda_r}$	2, $\forall r$	$m/4$
4. Free-Pinned 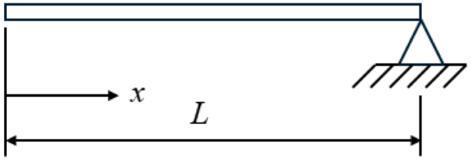	$\cosh\left(\frac{\lambda_r x}{L}\right)+\cos\left(\frac{\lambda_r x}{L}\right)$ $-\kappa_r\left(\sinh\left(\frac{\lambda_r x}{L}\right)+\sin\left(\frac{\lambda_r x}{L}\right)\right)$	$\tan\lambda_r - \tanh\lambda_r = 0$	$\frac{\cosh\lambda_r-\cos\lambda_r}{\sinh\lambda_r-\sin\lambda_r}$	2, $\forall r$	$m/4$
5. Pinned-Pinned 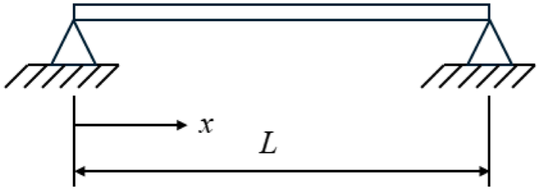	$\sin\left(\frac{\lambda_r x}{L}\right)$	$\cos\lambda_r + 1 = 0$	- -	1, $\forall r$	$m/2$

(*continued on next page*)

Table 1 (*continued*)

Case	$\widetilde{v}_r(x)$	Transcendental Equation for λ_r	κ_r	β_r	m_r
6. Sliding-Pinned 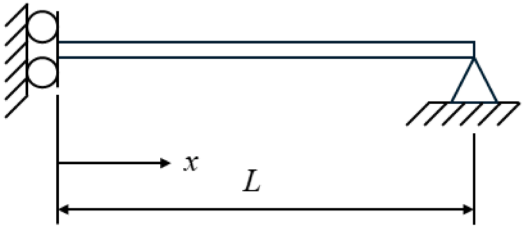	$\cos\left(\frac{\lambda_r x}{L}\right)$	$\cos\lambda_r = 0$	- -	$1, \ \forall r$	$m/2$
7. Sliding-Sliding 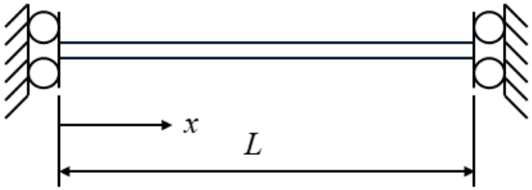	$\cos\left(\frac{\lambda_r x}{L}\right)$	$\sin\lambda_r = 0$	- -	$1, \ \forall r$	$m/2$
8. Clamped-Pinned 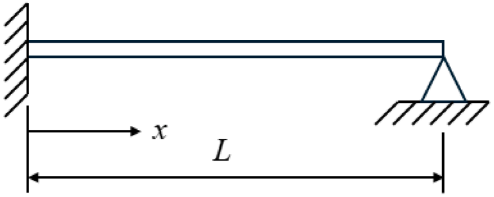	$\cosh\left(\frac{\lambda_r x}{L}\right) - \cos\left(\frac{\lambda_r x}{L}\right) -\kappa_r\left(\sinh\left(\frac{\lambda_r x}{L}\right) - \sin\left(\frac{\lambda_r x}{L}\right)\right)$	$\tan\lambda_r - \tanh\lambda_r = 0$	$\frac{\cosh\lambda_r - \cos\lambda_r}{\sinh\lambda_r - \sin\lambda_r}$	$1.509, \quad r = 1$ $1.512, \quad r = 2$ $1.512, \quad r = 3$ $1.512, \quad r = 4$	m/β_r^2
9. Clamped-Clamped 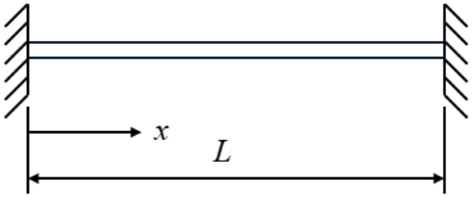	$\cosh\left(\frac{\lambda_r x}{L}\right) - \cos\left(\frac{\lambda_r x}{L}\right) -\kappa_r\left(\sinh\left(\frac{\lambda_r x}{L}\right) - \sin\left(\frac{\lambda_r x}{L}\right)\right)$	$\cos\lambda_r\cosh\lambda_r - 1 = 0$	$\frac{\cosh\lambda_r - \cos\lambda_r}{\sinh\lambda_r - \sin\lambda_r}$	$1.588, \quad r = 1$ $1.509, \quad r = 2$ $1.513, \quad r = 3$ $1.512, \quad r = 4$	m/β_r^2

(*continued on next page*)

Table 1 (*continued*)

Case	$\widetilde{v}_r(x)$	Transcendental Equation for λ_r	κ_r	β_r	m_r
10. Clamped-Sliding 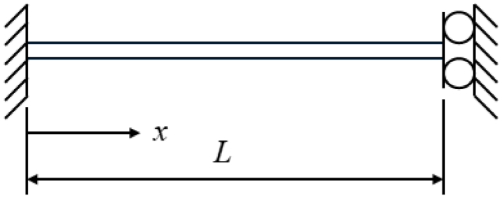	$\cosh\left(\frac{\lambda_r x}{L}\right) - \cos\left(\frac{\lambda_r x}{L}\right)$ $-\kappa_r\left(\sinh\left(\frac{\lambda_r x}{L}\right) - \sin\left(\frac{\lambda_r x}{L}\right)\right)$	$\tan\lambda_r + \tanh\lambda_r = 0$	$\frac{\sinh\lambda_r - \sin\lambda_r}{\cosh\lambda_r + \cos\lambda_r}$	1.588, $r = 1$ 1.513, $r = 2$ 1.512, $r = 3$ 1.512, $r = 4$	m/β_r^2

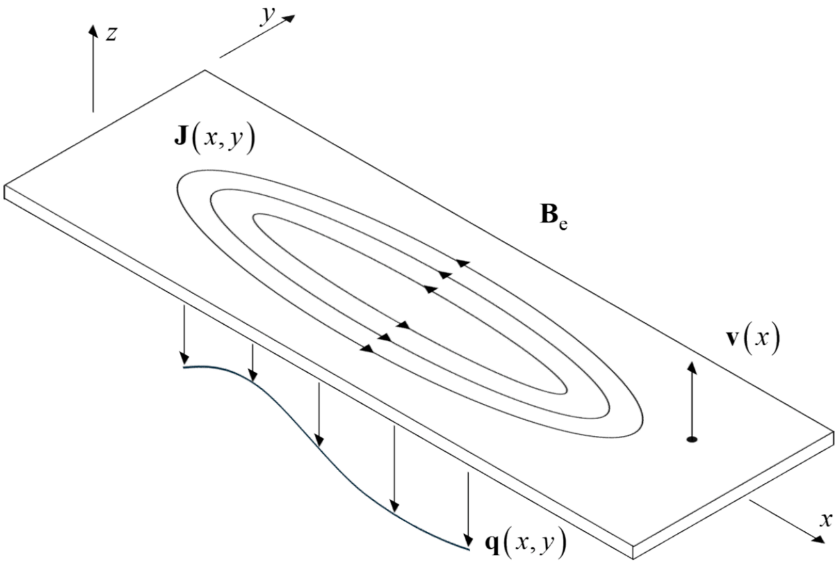

Fig. 1. Beam with eddy current damping under study for a free-free beam.

where $J_x(x,y)$ represents the spatial distribution of current density vector field in the x-direction, and $J_y(x,y)$ is its counterpart in the y-direction. Vibration is attenuated by the damping forces in the z-direction caused by the induced eddy currents. These forces can be represented as a pressure $\boldsymbol{q}(x,y)$, as illustrated in Fig. 1, originating from the Lorentz force. The dissipated power can be interpreted either as mechanical power dissipation or as electrical Joule losses in the form of heat [18].

The geometry of the beam is defined by its length L, width b, and thickness d, aligned with the x-, y-, and z-directions, respectively. The dimensions of the beam satisfy the condition $b < L$ and additionally, the beam is thin, meaning that $d \ll L$. The relevant material properties of the beam for the analysis presented in this work are its volumetric density ρ_v, Young's modulus E, and electrical resistivity ρ, all of which are uniform throughout the entire beam.

The external magnetic field is uniform and static (or time-invariant), characterised by the magnetic flux density vector $\boldsymbol{B}_\mathrm{e} = B\widehat{\boldsymbol{x}}$, where B represents its magnitude. Only the magnetic field in the x-direction is considered, as it is the sole term responsible for inducing eddy currents when bending mode vibrations are applied [18].

In this work, the velocity spatial distribution $v(x)$ is associated with bending mode shapes, and for the r-th mode, this results in

$$v_r(x) = v_\mathrm{max}\frac{\widetilde{v}_r(x)}{\beta_r}, \tag{2}$$

where v_max is the maximum velocity, and $\widetilde{v}_r(x)$ is the mode shape, provided in Table 1 [22] for the ten boundary conditions to study. In this table, λ_r is the eigenvalue of the r-th mode, κ_r is a coefficient, and β_r is a normalisation factor of the mode shape $\widetilde{v}_r(x)$. The information in Table 1 shows that the normalisation factor β_r is a natural number (either 2 or 1) for all modes, except for cases 8, 9 and 10, where it is a positive real number. Only three decimal places are shown for this factor; however, it can be determined more accurately from the derivative of the mode shape.

Another important magnitude for the r-th mode presented in Table 1, is the modal mass of the beam m_r, which represents the equivalent mass of a single-degree-of-freedom system containing the same kinetic energy as the vibrating mass and is related with the beam's mass m ($m = \rho_\mathrm{v}Lbd$). The ratio of the beam's mass to its modal mass is a natural number (either 4 or 2) for all boundary conditions, except in cases 8, 9 and 10, where it is given by β_r^2.

The harmonic bending motion of the beam, for the r - th mode, occurs at an angular natural frequency ω_r, which can be obtained as [22]

$$\omega_r = \frac{\lambda_r^2 d}{L^2}\sqrt{\frac{E}{12\rho_\mathrm{v}}} \tag{3}$$

Eddy currents are induced due to the interaction between the harmonic motion and the external magnetic field. Since the vibration is harmonic, the resulting eddy currents are also harmonic and occur at the same angular natural frequency ω_r, as the motion is in steady state. As Eq. (1) indicates, the spatial distribution of the current density vector field $\boldsymbol{J}(x,y)$ is only generated in the x - y plane, given the small thickness of the beam. This assumption is valid only if, for the r - th mode, the skin depth δ_r given by [1]

$$\delta_r = \sqrt{\frac{2\rho}{\mu_0 \omega_r}}, \tag{4}$$

where μ_0 is the permeability of free space, is sufficiently large relative to the beam thickness. This implies that the condition $\delta_r > d$ must hold.

3. Electromechanical model of the beam with eddy current damping and its equivalent Kelvin-Voight mechanical model

The system introduced in Section 2, where eddy currents are induced via motional induction, and depicted in Fig. 1 for a free-free beam, can be modelled as an electromechanical system, as shown in Fig. 2. This model applies when self-inductance is neglected and is valid for any beam boundary condition [19]. For this model, self-inductance is negligible when the reactance ωL_s is significantly smaller than the resistance R, ensuring that the system behaves primarily as a resistive circuit, where ω denotes the angular velocity and L_s represents the coefficient of self-induction. This condition requires that either ω and/or L_s must be sufficiently small. Since velocity and frequency are related by $v = \omega A$, where A represents the vibration amplitude, the condition

$$v \ll \frac{R}{L_s} A \tag{5}$$

must be satisfied. To determine a velocity threshold beyond which self-induction effects can be neglected, it is necessary to estimate both R and L_s. In a previous study by Siakavellas [23], analytical expressions for both R and L_s are provided for a rectangular plate, although it is assumed that the currents circulate in rectangular paths, rather than in closed, curved loops as is the case in this work. However, by assuming that $L \gg b$, which is a reasonable assumption for the system in this study, the expressions provided by Siakavellas can be regarded as sufficiently accurate for determining a velocity limit in Eq. (5) beyond which self-inductance effects are neglected for the beam. Thus, Eq. (5) can be rewritten as [23]

$$v \ll \frac{6\pi\rho A}{\mu_0 b d (1 + 2\ln 2)}. \tag{6}$$

If small vibration amplitudes are considered, then self-inductance effects are neglected when Eq. (6) is satisfied. Eq. (6) has been verified for all cases of Sections 5 and 6.

In this electromechanical representation, the non-magnetic conducting beam is modelled as a bar of equivalent mass m_{eq} and length ℓ, connected to a spring of stiffness k. The length ℓ represents the equivalent length of the conductor and is related to the shape of the eddy current density maps induced in the beam. Similar to the original beam, the bar is subjected to a uniform, static external magnetic field of magnitude B in the x-direction and vibrates in the z-direction with a velocity magnitude $v_{\max}$ and angular frequency ω. Motional induction generates a current I in a closed loop C, which includes an electrical resistance R. The equation of motion for this model is expressed as [19]

$$m_{\text{eq}}\ddot{u}(t) + \frac{B^2\ell^2}{R}\dot{u}(t) + ku(t) = 0, \tag{7}$$

where t represents time, $(\dot{\bullet})$ denotes time derivative, and $u(t)$ represents the displacement of the moving bar. Here, $\dot{u}_{\max}$ is equivalent to the mode shape magnitude $v_{\max}$.

The electromechanical model in Fig. 2 is equivalent to the Kelvin-Voight damping mechanical model depicted in Fig. 3 [19].

In this single-degree-of-freedom mechanical model, the beam is represented by a block of equivalent mass m_{eq}, connected to a

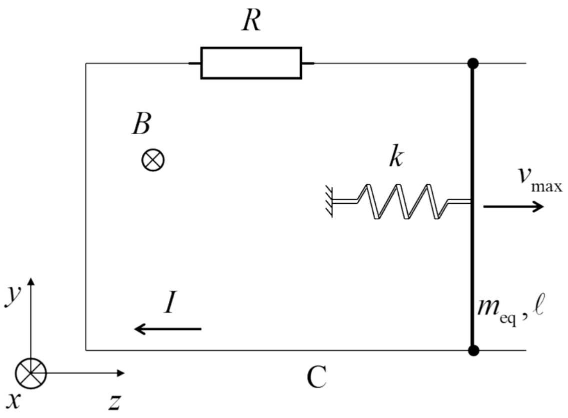

Fig. 2. Electromechanical model of the beam with eddy current damping.

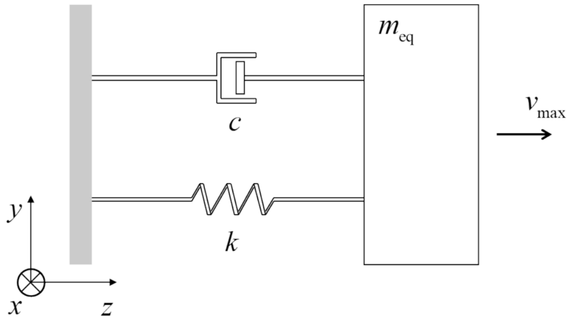

Fig. 3. Equivalent Kelvin-Voight damping mechanical model.

spring of stiffness k and a dashpot with viscous coefficient c. The block vibrates in the z-direction with a velocity magnitude $v_{\max}$ and angular frequency ω. The corresponding equation of motion is given by

$$m_{\mathrm{eq}}\ddot{u}(t)+c\dot{u}(t)+ku(t)=0 \tag{8}$$

By comparing the equations of motion for the electromechanical model given by Eq. (7) and the mechanical model given by Eq. (8), their equivalence is evident. The equivalent mass and spring stiffness are identical in both models. Furthermore, the viscous coefficient c in the Kelvin-Voight model is related to the coefficients of the electromechanical system through the following relationship

$$c=\frac{B^2\ell^2}{R}, \tag{9}$$

which links c to the external magnetic field B, the bar length ℓ, and the electrical resistance R in Fig. 2. Additionally, from the model in Fig. 3, the viscous damping ratio ζ of a single-degree-of-freedom system can be defined as

$$\zeta=\frac{c}{2\sqrt{km_{\mathrm{eq}}}} \tag{10}$$

These models, and their equivalence, provide significant insights into the damping behaviour of the original beam. The analysis can be approached from the perspective of the electromechanical model in Fig. 2, once m_{eq}, k, R, I, and ℓ are established, or from the perspective of the equivalent Kelvin-Voight mechanical model in Fig. 3 by specifying m_{eq}, k, and c.

4. Numerical procedure for solving eddy currents for motional induction and output variables

The eddy currents induced by the interaction between the beam's vibration and the external magnetic field must be determined in order to calculate the output variables. This Section begins with the presentation of the electromagnetic equations governing motional induction, followed by a detailed explanation of the numerical procedure employed to solve for the eddy currents. It concludes with a description of the output variables to be derived in the analysis, obtained once the eddy currents are solved.

4.1. Electromagnetic equations

The dynamic behaviour of the generic beam depicted in Fig. 1 is governed by the general expression of Faraday's law of induction. In its quasi-static form, this law is expressed in integral form as [1]

$$\oint_{\mathrm{C}}(\rho\boldsymbol{J})\cdot\mathrm{d}\boldsymbol{l}=-\int_{\mathrm{S}}\dot{\boldsymbol{B}}_{\mathrm{i}}\cdot\mathrm{d}\boldsymbol{S}-\int_{\mathrm{S}}\dot{\boldsymbol{B}}_{\mathrm{e}}\cdot\mathrm{d}\boldsymbol{S}+\oint_{\mathrm{C}}(\boldsymbol{v}\times\boldsymbol{B}_{\mathrm{e}})\cdot\mathrm{d}\boldsymbol{l}, \tag{11}$$

where $\boldsymbol{B}_{\mathrm{i}}$ represents the magnetic field density vector induced by the eddy currents through self-inductance, $\boldsymbol{B}_{\mathrm{e}}$ is the external magnetic field density vector, $\boldsymbol{v}$ is the velocity field vector, C is an arbitrary contour within the domain, S is the surface enclosed by the arbitrary contour C, $\mathrm{d}\boldsymbol{l}$ is an elementary distance vector along the contour C, $\mathrm{d}\boldsymbol{S}$ is an elementary surface area vector of the surface S, $\cdot$ denotes the dot product, and $\times$ denotes the cross product. In this study $\dot{\boldsymbol{B}}_{\mathrm{i}}=\boldsymbol{0}$, because the beam is thin, and this parametric study focuses on lower frequencies, where self-inductance effects are not significant [24]. Additionally, $\dot{\boldsymbol{B}}_{\mathrm{e}}=\boldsymbol{0}$ since the external magnetic field is time-invariant in this work.

It is important to note that in Eq. (11) the modal bending velocity is time-dependent; however, in this study, it is harmonic, with $\boldsymbol{v}$ representing its spatial distribution as indicated in Eq. (2). Given that the resulting variables associated with the velocity, such as the currents, are also harmonic, for the sake of convenience, from this point forward, all vector terms in subsequent equations will refer to their spatial distributions.

The principle of charge conservation must be satisfied throughout the beam, leading to the steady-state continuity equation for currents

$$\nabla \cdot \boldsymbol{J} = 0, \tag{12}$$

where ∇ is the del operator $\nabla = \frac{\partial}{\partial x}\widehat{\boldsymbol{x}} + \frac{\partial}{\partial y}\widehat{\boldsymbol{y}} + \frac{\partial}{\partial z}\widehat{\boldsymbol{z}}$, and $\nabla\cdot$ represents the divergence operator. This equation indicates that the current density vector is divergence-free, and therefore, there exists a vector potential $\boldsymbol{T}$ from which the current density vector can be expressed as [25]

$$\boldsymbol{J} = \nabla \times \boldsymbol{T}, \tag{13}$$

where $\nabla\times$ represents the curl operator. As the beam is thin, and the Euler-Bernoulli beam theory is employed for its mechanical behaviour, the vector potential $\boldsymbol{T}$ is defined solely in the z-direction, i.e., $\boldsymbol{T}(x,y) = T(x,y)\widehat{\boldsymbol{z}}$, where $T(x,y)$ is the spatial distribution of the vector potential $\boldsymbol{T}$. Substituting Eq. (13) into Eq. (11) yields

$$\oint_{\mathrm{C}} (\rho \nabla \times \boldsymbol{T}) \cdot \mathrm{d}\boldsymbol{l} = \oint_{\mathrm{C}} (\boldsymbol{v} \times \boldsymbol{B}_{\mathrm{e}}) \cdot \mathrm{d}\boldsymbol{l} \tag{14}$$

To solve Eq. (14) and obtain $\boldsymbol{T}$, boundary conditions must be applied. It has been demonstrated that, due to the relationship between $\boldsymbol{J}$ and $\boldsymbol{T}$ given in Eq. (13), selecting any arbitrary constant along the beam's edge satisfies Eq. (12) [26]. For mathematical simplicity, in this work, $T(x,y) = 0$ is chosen along the beam's edge. As Eq. (14) lacks an analytical solution, numerical methods must be utilised. The numerical procedure for solving the currents is presented below.

4.2. Numerical method

The aim of the numerical procedure is to determine the current density vector $\boldsymbol{J}$ throughout beam's surface. To achieve this, the vector potential $\boldsymbol{T}$ is first solved from Eq. (14), and then $\boldsymbol{J}$ is obtained using the definition given in Eq. (13). The numerical method used to solve $\boldsymbol{T}$ from Eq. (14) is based on the finite differences method developed by Nagel, which allows for the calculation of $\boldsymbol{T}$ in a metallic, non-magnetic sheet subjected to a time-varying magnetic field [26]. This method has been recently extended to include the effects of motional induction [18], and the same procedure is employed here. A brief description of the method follows, with further details available in [18].

The surface of the beam is discretised into N rectangular cells, with N_x cells along the x-direction and N_y cells along the y-direction. Each cell represents a rectangular block with uniform current density $\boldsymbol{J}$, with length h_x in the x-direction, width h_y in the y-direction, and thickness d in the z-direction. Fig. 4 illustrates an example of the discretisation scheme in the x - y plane, with the contour integral from Eq. (14) represented by the dashed line. Here, the current density $\boldsymbol{J}$, and velocity field $\boldsymbol{v}$ are defined at the centre of each cell, indicated by crosses × in Fig. 4, while the electric vector potential $\boldsymbol{T}$ is defined at the cell corners, marked by dots • in Fig. 4.

Integration of Eq. (14) for any node T_0 within the discretisation scheme, as shown by the dashed contour in Fig. 4 and detailed further in Fig. 5, yields (for more information on the resolution process, see [18,26,27])

$$\rho\left[\frac{h_x}{h_y}(2T_0 - T_2 - T_4) + \frac{h_y}{h_x}(2T_0 - T_1 - T_3)\right] = h_y B(v_2 - v_1), \tag{15}$$

where T_i are the potentials at each node of the five-point star depicted in Fig. 5, where $\mathrm{d}\boldsymbol{l}_i$ is the elemental vector distance associated with each side of the dashed line, v_1 is the velocity of the left-side corners of the contour and v_2 is the equivalent velocity for the right-side corners. On each side, the velocity at the left or right corners is the identical, as the applied velocity field from Eq. (2) does not vary in the y-direction.

Eq. (15) is applied to each internal T node, assembling a linear system of equations. However, without boundary conditions, the system is indeterminate. As mentioned earlier, $T(x,y) = 0$ along the beam's edge. Thus, the vector potential $\boldsymbol{T}$ is divided between the edge nodes $\boldsymbol{T}_{\mathrm{edge}}$, and the unknowns $\boldsymbol{T}_{\mathrm{uk}}$, i.e. $\boldsymbol{T} = \{\boldsymbol{T}_{\mathrm{edge}} \quad \boldsymbol{T}_{\mathrm{uk}}\}^{\mathrm{T}}$, where $\{\bullet\}^{\mathrm{T}}$ represents the transpose operator, and $\boldsymbol{T}_{\mathrm{edge}} = \boldsymbol{0}$. As a

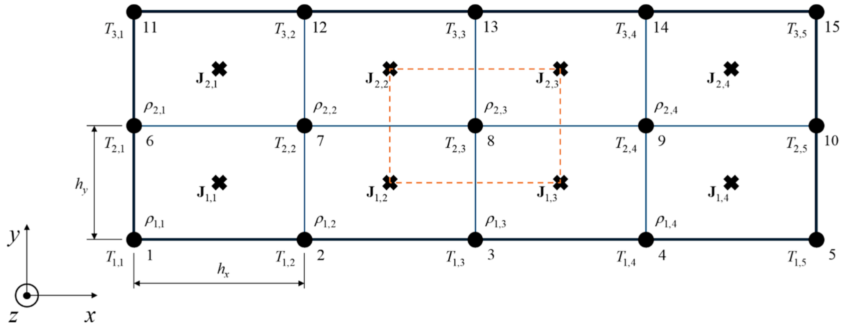

Fig. 4. Example of beam discretisation.

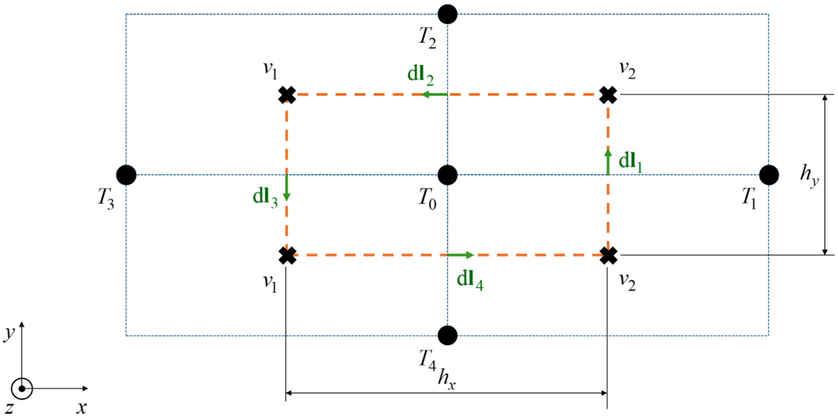

Fig. 5. Integration domain of a node.

result, a linear system of $(N_x-1)(N_y-1)$ equations is formed, from which $\boldsymbol{T}_{\mathrm{uk}}$ is obtained from

$$\boldsymbol{M}\boldsymbol{T}_{\mathrm{uk}} = \boldsymbol{b}, \tag{16}$$

where $\boldsymbol{M}$ is a symmetric coefficient matrix assembled from the left-hand side of Eq. (15), and $\boldsymbol{b}$ is the vector of independent terms assembled from the right-hand side of Eq. (15). Finally, the current density $\boldsymbol{J}$ for each cell is calculated using Eq. (13), yielding

$$J_x = \frac{-T_1 - T_2 + T_3 + T_4}{2h_y} \tag{17}$$

and

$$J_y = \frac{-T_1 + T_2 - T_3 + T_4}{2h_x} \tag{18}$$

These equations allow for the calculation of the current density $\boldsymbol{J}$ for each of the N cells.

4.3. Parametric study output variables

After solving the current equations, the output variables of the parametric study can be computed. Specifically, the electrical variables include the maximum current density, the average dissipated power, and the total current. The structural variables are the angular natural frequency and stiffness. Additionally, the coefficients of the electromechanical model consist of the electrical resistance and bar length, while those of the Kelvin-Voight mechanical model include the viscous coefficient and the viscous damping ratio. The procedure for computing these output variables is outlined below.

4.4. Average dissipated power

The induced eddy currents dissipate power as heat within the material, a phenomenon known as Joule's heating, which can be expressed by the differential form of Joule's law [28] as

$$p(x,y,t) = \rho \boldsymbol{J}_{\mathrm{ins}}(x,y,t) \cdot \boldsymbol{J}_{\mathrm{ins}}(x,y,t), \tag{19}$$

where t denotes time, $p(x,y,t)$ represents the instantaneous dissipated power per unit volume, and $\boldsymbol{J}_{\mathrm{ins}}(x,y,t)$ represents the instantaneous eddy current density vector field. Since the current density is harmonic in this work, the above expression can be averaged over a cycle, yielding

$$\overline{p} = \rho \frac{\boldsymbol{J}(x,y) \cdot \boldsymbol{J}(x,y)}{2}, \tag{20}$$

where $\overline{p}$ is the average dissipated power per unit volume, and the factor of 2 accounts for the averaging of the harmonic functions. The average power dissipated per unit volume at the centre of the j - th cell can be calculated from Eq. (20) by taking the eddy current density at that point from the terms in Eq. (17) and Eq. (18). This resulting power is constant throughout the cell volume, as the eddy current density is also constant. The total average dissipated power P in the beam is then computed by summing the contribution of each individual cell over the beam's surface [18], resulting, for the $\boldsymbol{r}$-th mode, in

$$P_r = \rho h_x h_y d \sum_{j=1}^{N} \frac{J_{x_r}^2\left(x_j, y_j\right) + J_{y_r}^2\left(x_j, y_j\right)}{2}, \tag{21}$$

where x_j and y_j refer to the x- and y-coordinates of the centre of the j - th cell.

4.5. Total current circulating in the beam

The total current circulating in the beam I can be derived from the current density $\boldsymbol{J}$. It is known that for modal bending motion, the induced eddy currents are symmetric about the longitudinal axis of the beam [18]. Furthermore, due to the charge conservation principle presented in Eq. (12), the following integral

$$d \int_0^L J_y \mathrm{d}x = 0 \tag{22}$$

along the longitudinal axis of the beam must be equal to zero. In the finite difference scheme used to compute the eddy current density $\boldsymbol{J}$, since the current density is constant within each cell, the total current I can be calculated, for the r-th mode, as

$$I_r = dh_x \sum_{k=1}^{N_x} J_{y_r}^{+}\left(x_k^{+}, 0\right) = dh_x \sum_{k=1}^{N_x} \left| J_{y_r}^{-}\left(x_k^{-}, 0\right) \right|, \tag{23}$$

where $J_{y_r}^{+}$ denotes the positive current density along the cells on the beam's axis for the r-th mode, x_k^{+} is the x-coordinate of the centre of a cell corresponding to the positive values of $J_{y_r}^{+}$, and $J_{y_r}^{-}$ and x_k^{-} represent the analogous negative values of J_{y_r}. The notation $|\bullet|$ represents the absolute value. The total sum of the individual numerical values of $J_{y_r}^{+}$ and $J_{y_r}^{-}$ must be equal, as evidenced by Eq. (23) and illustrated by the schematic diagram in Fig. 6.

4.6. Stiffness

For any of the models in Fig. 2 and in Fig. 3, since the vibration is given by the mode shape given in Eq. (2), for each r-th mode, vibration occurs at the corresponding angular natural frequency ω_r, described in Eq. (3). Then, the equivalent mass of the models corresponds to the modal mass m_r (see Table 1) and the stiffness of the r-th mode is given by

$$k_r = \omega_r^2 m_r \tag{24}$$

It is important to note that, in a general sense, the stiffness in the above expression is calculated from the equivalent mass m_{eq}, as given in the models in Figs. 2 and 3. However, since this work focuses entirely on resonance, for the r-th mode it is stablished that $m_r \equiv m_{\mathrm{eq}}$.

4.7. Electrical resistance

The circulating currents induced within the beam as a result of its motion in the presence of a magnetic field dissipate energy as heat. This energy dissipation corresponds to an effective electrical resistance, which arises from the interaction between the induced currents and the material's inherent resistivity. For the r-th mode, the electrical resistance of the beam R and corresponding to the one in the electromechanical model in Fig. 2, is determined using Joule's law as [1]

$$R_r = \frac{2P_r}{I_r^2}, \tag{25}$$

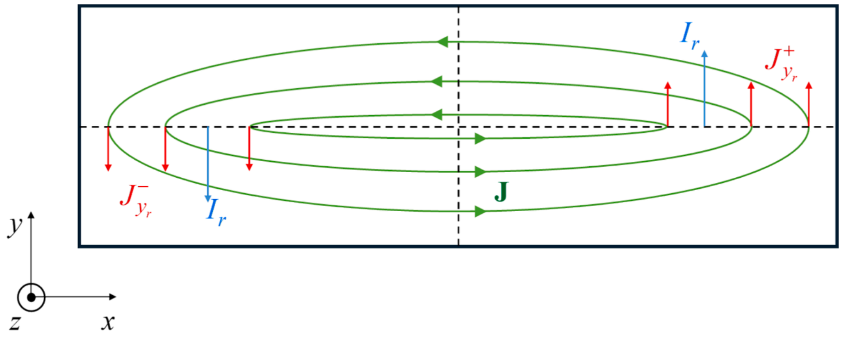

Fig. 6. Scheme for calculating the total current circulating in the beam.

where the factor of 2 accounts for the root mean square (RMS) current circulating in the beam.

4.8. Bar length

From the power dissipated by the Lorentz force, bar length ℓ of the electromechanical model can be deduced. For the r-th mode, the length results in [19]

$$\ell_r = \frac{2P_r}{Bv_{\max}I_r} \tag{26}$$

4.9. Viscous coefficient

For the r-th mode, and in accordance with Eq. (9), the viscous coefficient c_r can be expressed as

$$c_r = \frac{B^2\ell_r^2}{R_r} \tag{27}$$

4.10. Viscous damping ratio

In the Kelvin-Voight mechanical model depicted in Fig. 3, an equivalence can be made between the Joule's losses of the eddy currents and the energy dissipated by the dashpot as

$$P = \frac{1}{2}cv_{\max}^2 \tag{28}$$

Thus, for the r-th mode, the viscous damping ratio ζ_r is derived as [18]

$$\zeta_r = \frac{P_r}{m_r\omega_r v_{\max}^2}. \tag{29}$$

5. Analysis of the nature of the eddy currents for motional induction

This Section presents an analysis of the eddy current density maps obtained for the reference beam with the clamped-free and sliding-pinned boundary conditions, corresponding to cases 3 and 6 in Table 1. These two cases analyse, taken as examples from the ten types of boundary conditions listed in Table 1, combinations of the four different types of boundary conditions (free, clamped, sliding and pinned). The aim is to examine how these types of boundary conditions influence the behaviour of the currents and generalise these findings to the other cases in Table 1. These maps and those of the remaining beam boundary conditions listed in Table 1 are provided in Appendix.

The beam's vibration is characterised by bending mode shapes, with eddy currents induced by an externally applied uniform and constant magnetic field. First, the geometry and material properties of the reference beam are described. Then, a study of the eddy current maps is conducted, and the nature of the currents is analysed for the different boundary conditions.

5.1. Model data of the reference beam

This section outlines the geometry and material properties of the reference beam, along with general considerations regarding the discretisation.

The beam's geometry and corresponding uniform material properties are detailed in Table 2, where the electrical conductivity is defined as $\sigma = 1/\rho$. Aluminium is selected as the non-magnetic conducting material due to its high conductivity.

The external magnetic field is applied in the x-direction with a magnitude of $B = 1$ T. The beam's motion is characterised by the r - th bending mode shape, as described in Eq. (2), with $v_{\max} = 1$ m/s. The discretisation of the beam follows the procedure outlined in Section 3.2, consisting of 421 rectangular cells along the x-direction and 21 rectangular cells along the y-direction. In the following analysis of the eddy current density maps, the first four bending modes are examined, with maps provided for four evenly spaced beam

Table 2
Reference beam geometry and material properties.

Property	Value
b(mm)	10
d(mm)	1
$\rho_v\left(\mathrm{kg/m^3}\right)$	2700
E (GPa)	65
σ(MS/m)	5

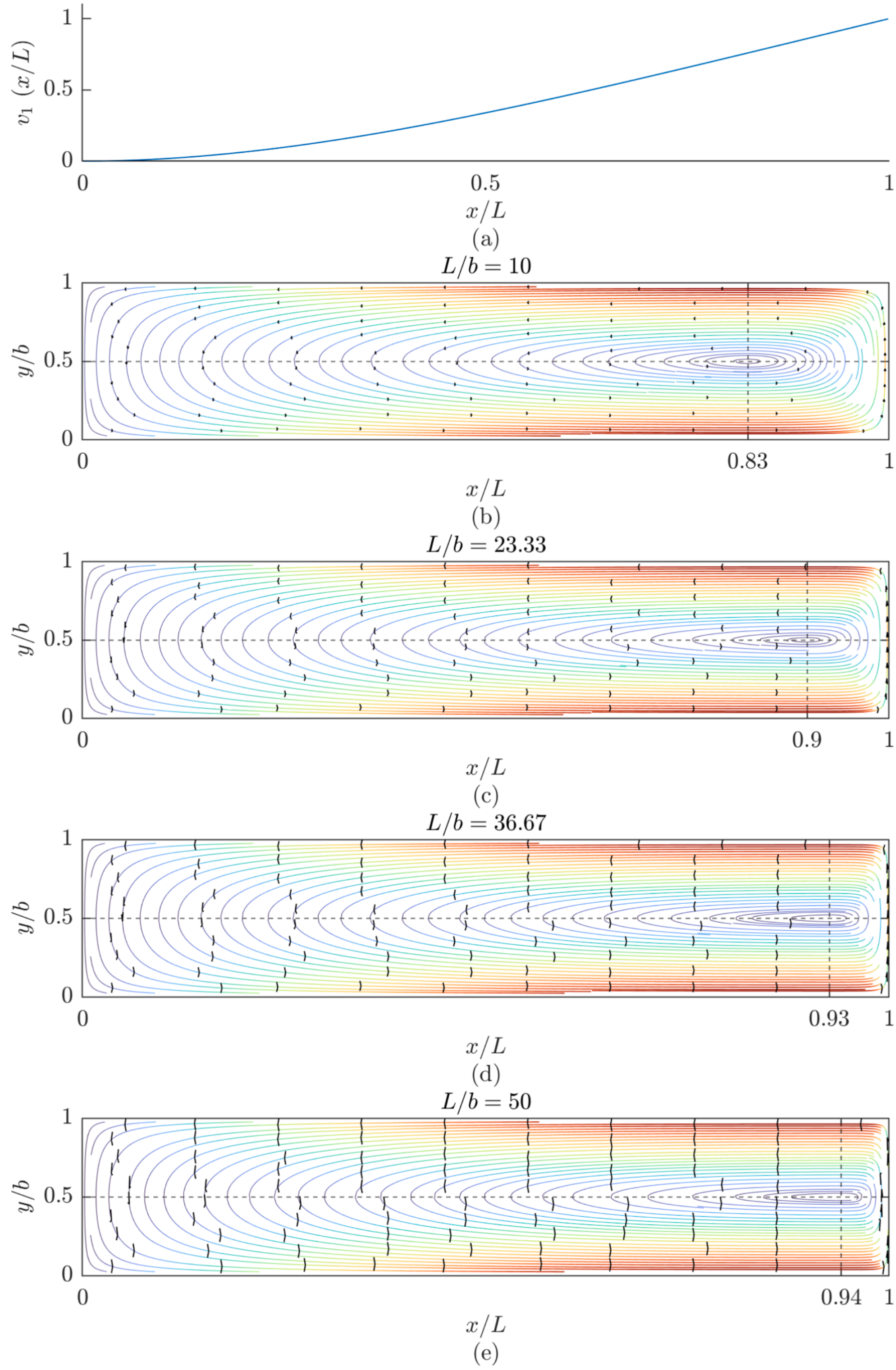

Fig. 7. Eddy current density maps for the first bending mode of the clamped-free reference beam: (a) modal velocity; (b) eddy current density map for $L/b = 10$; (c) eddy current density map for $L/b = 23.33$; (d) eddy current density map for $L/b = 36.67$ and (e) eddy current density map for $L/b = 50$.

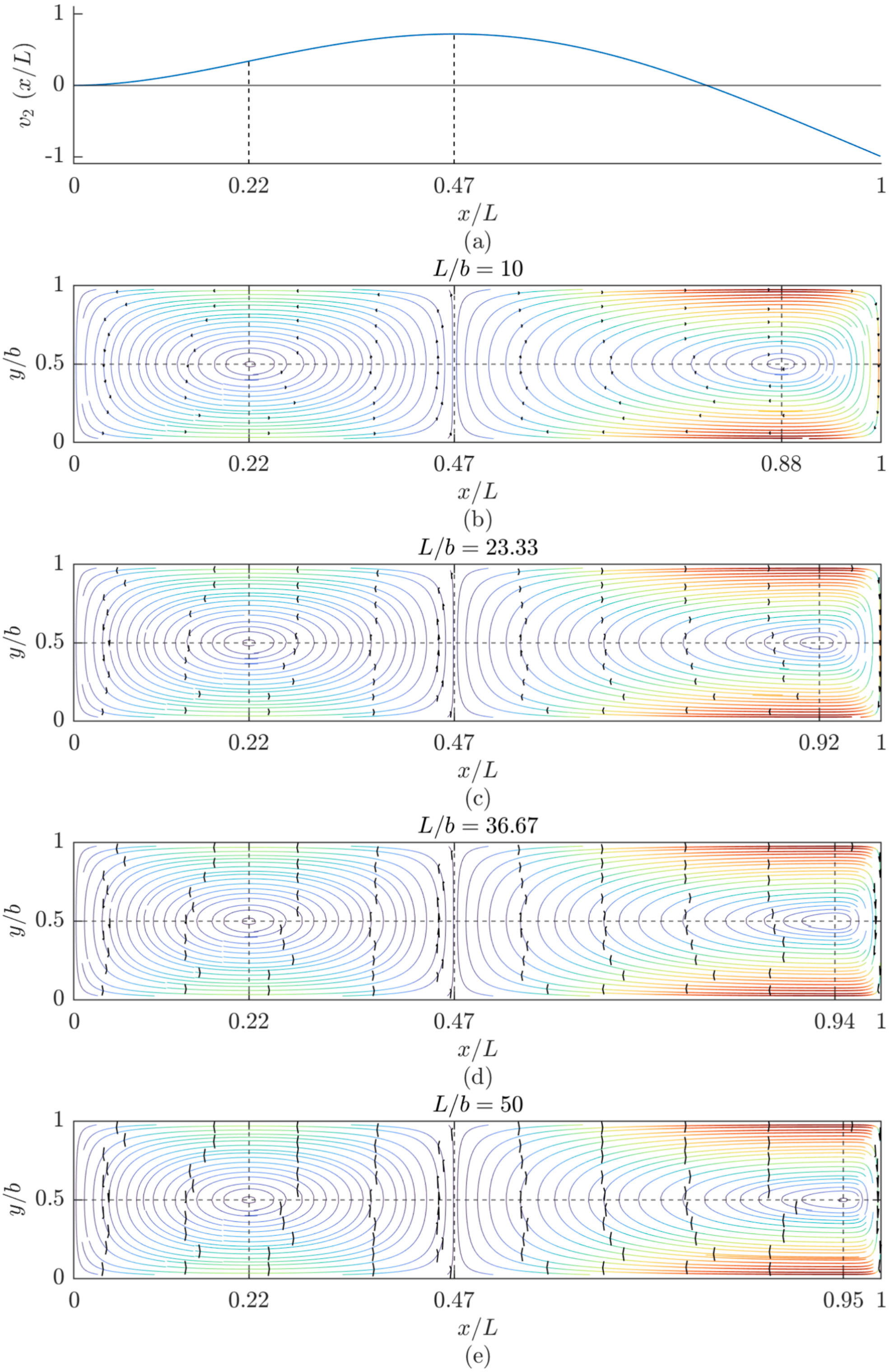

Fig. 8. Eddy current density maps for the second bending mode of the clamped-free reference beam: (a) modal velocity; (b) eddy current density map for $L/b = 10$; (c) eddy current density map for $L/b = 23.33$; (d) eddy current density map for $L/b = 36.67$ and (e) eddy current density map for $L/b = 50$.

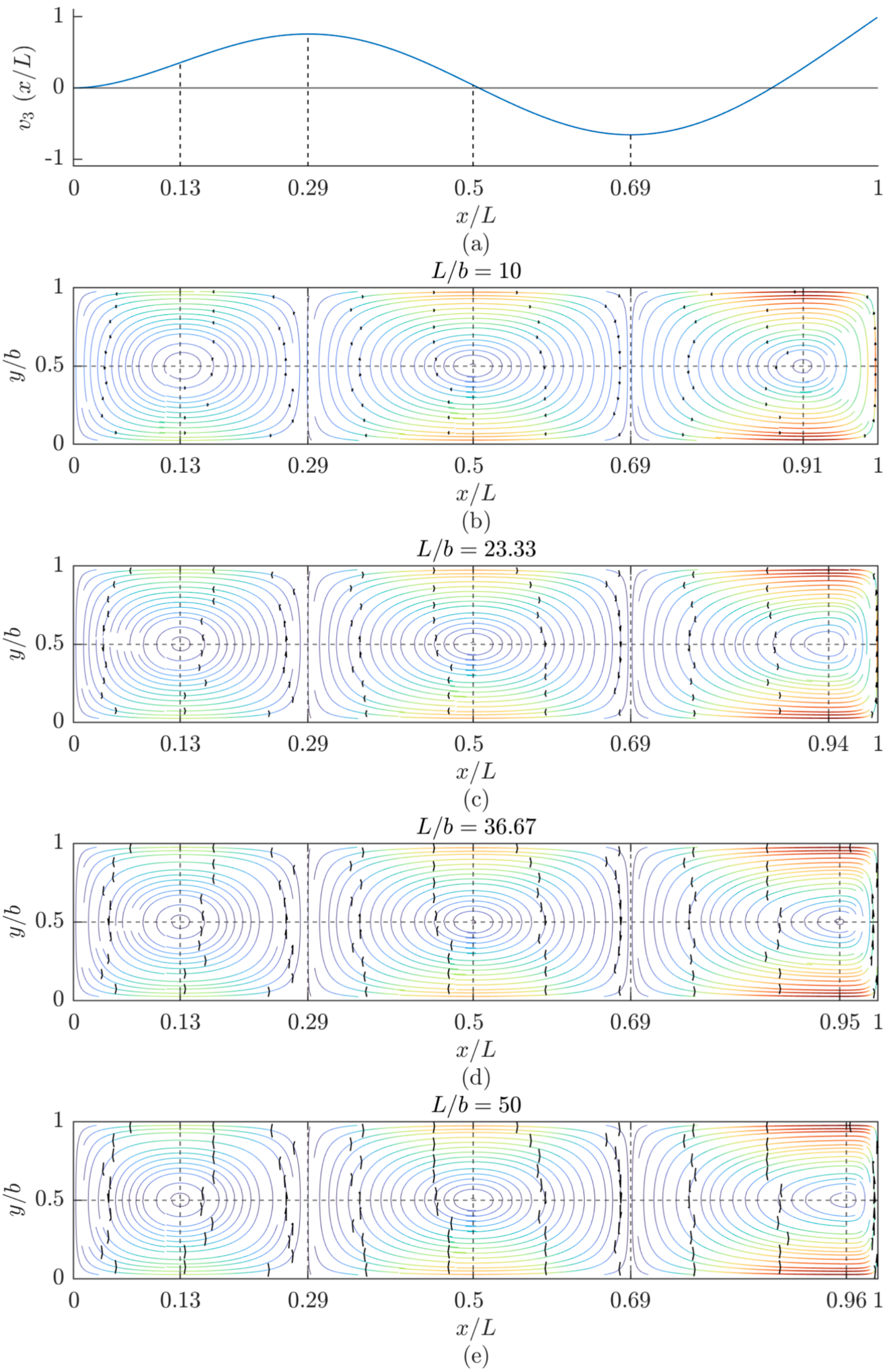

Fig. 9. Eddy current density maps for the third bending mode of the clamped-free reference beam: (a) modal velocity; (b) eddy current density map for $L/b = 10$; (c) eddy current density map for $L/b = 23.33$; (d) eddy current density map for $L/b = 36.67$ and (e) eddy current density map for $L/b = 50$.

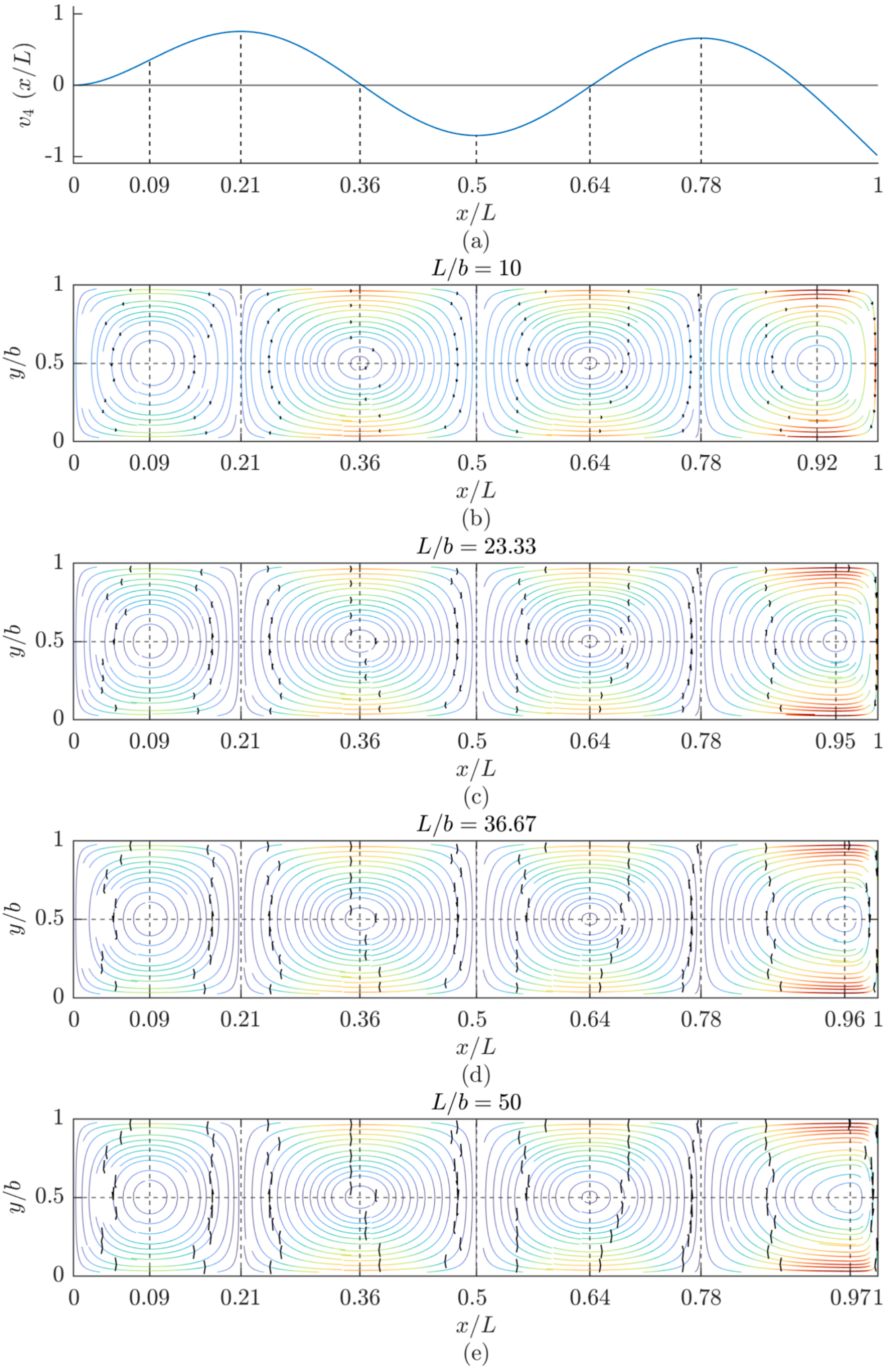

Fig. 10. Eddy current density maps for the fourth bending mode of the clamped-free reference beam: (a) modal velocity; (b) eddy current density map for $L/b = 10$; (c) eddy current density map for $L/b = 23.33$; (d) eddy current density map for $L/b = 36.67$ and (e) eddy current density map for $L/b = 50$.

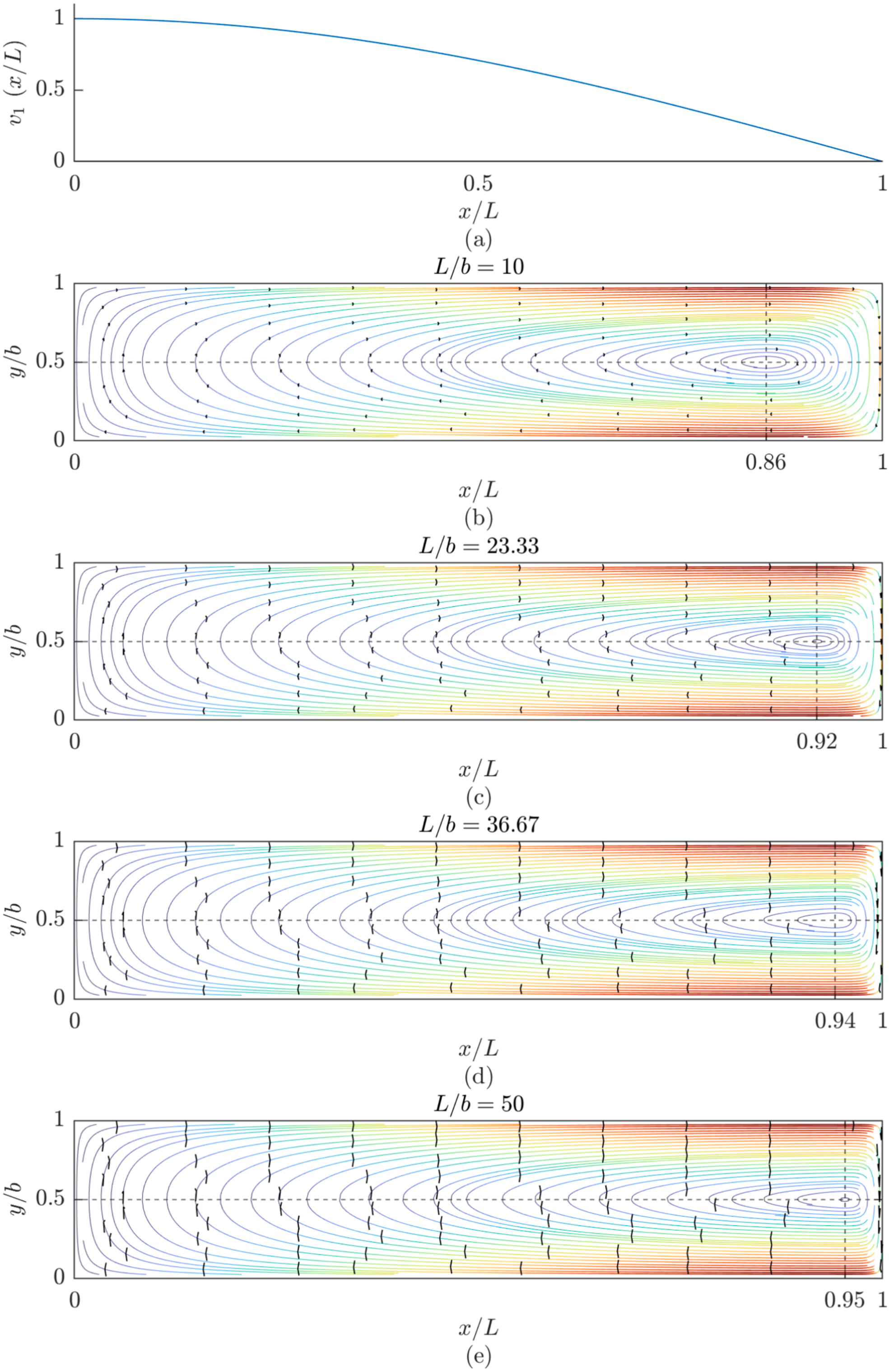

Fig. 11. Eddy current density maps for the first bending mode of the sliding-pinned reference beam: (a) modal velocity; (b) eddy current density map for $L/b = 10$; (c) eddy current density map for $L/b = 23.33$; (d) eddy current density map for $L/b = 36.67$ and (e) eddy current density map for $L/b = 50$.

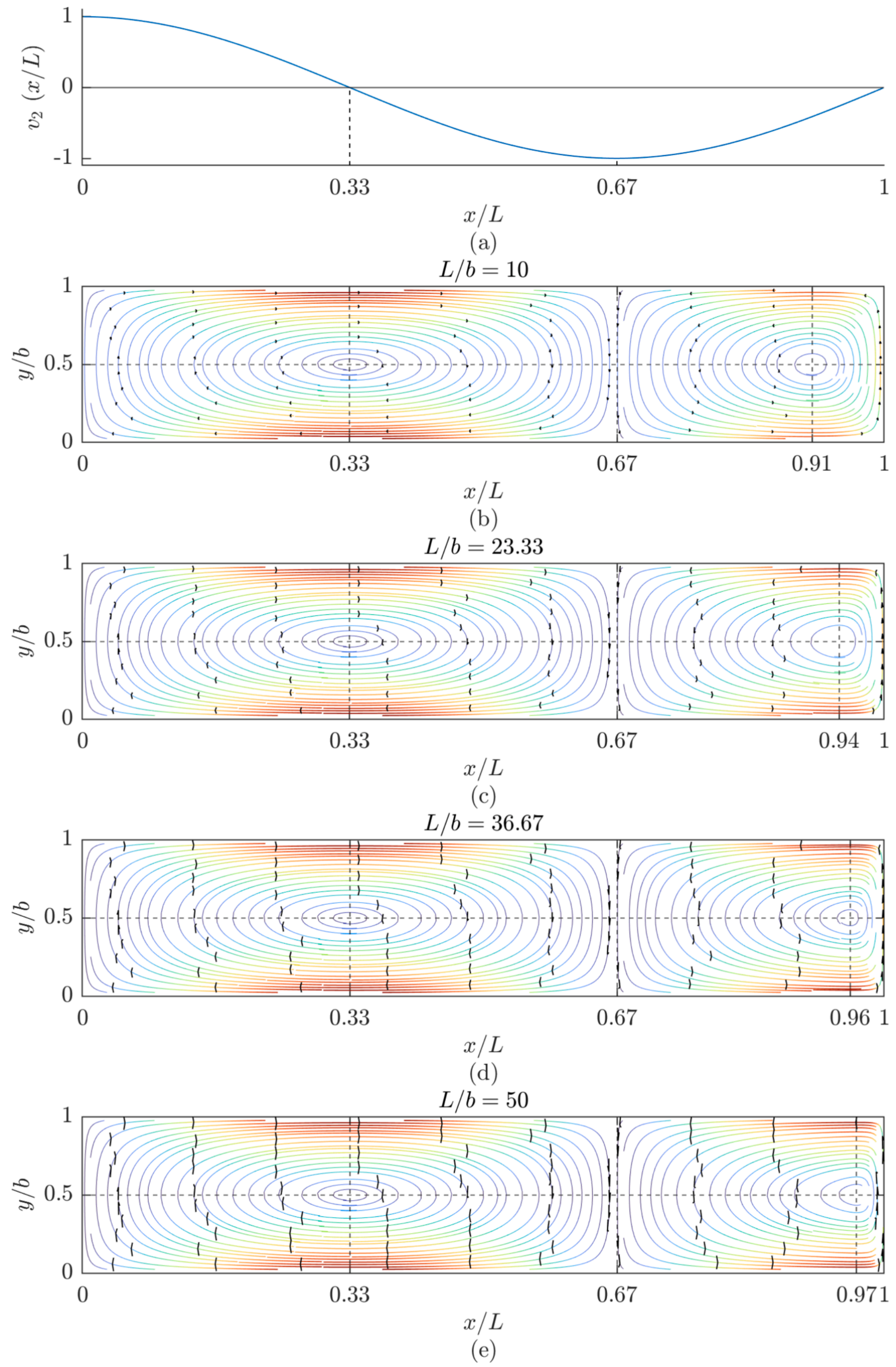

Fig. 12. Eddy current density maps for the second bending mode of the sliding-pinned reference beam: (a) modal velocity; (b) eddy current density map for $L/b = 10$; (c) eddy current density map for $L/b = 23.33$; (d) eddy current density map for $L/b = 36.67$ and (e) eddy current density map for $L/b = 50$.

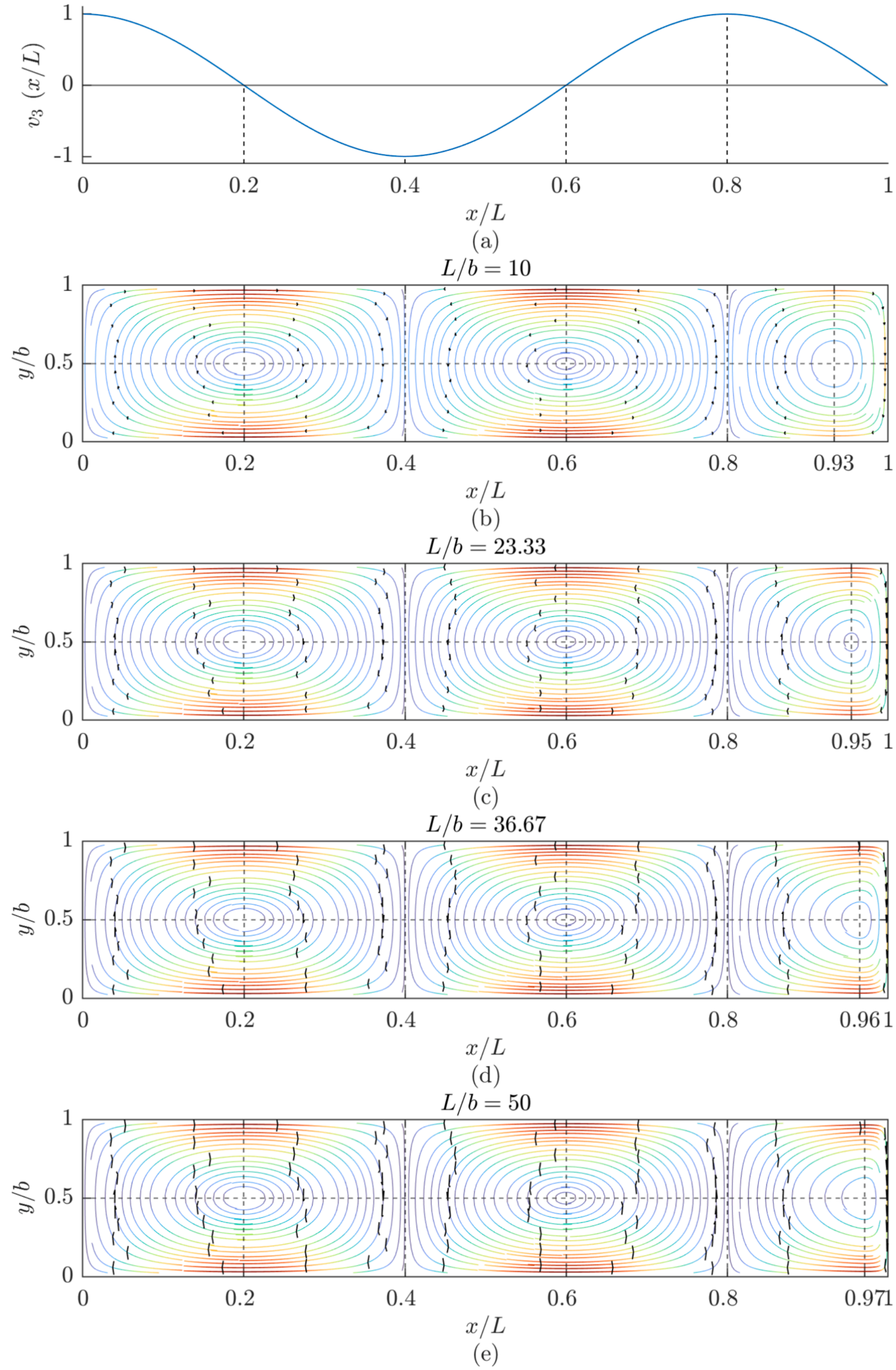

Fig. 13. Eddy current density maps for the third bending mode of the sliding-pinned reference beam: (a) modal velocity; (b) eddy current density map for $L/b\ = 10$; (c) eddy current density map for $L/b\ = 23.33$; (d) eddy current density map for $L/b = 36.67$ and (e) eddy current density map for $L/b\ = 50$.

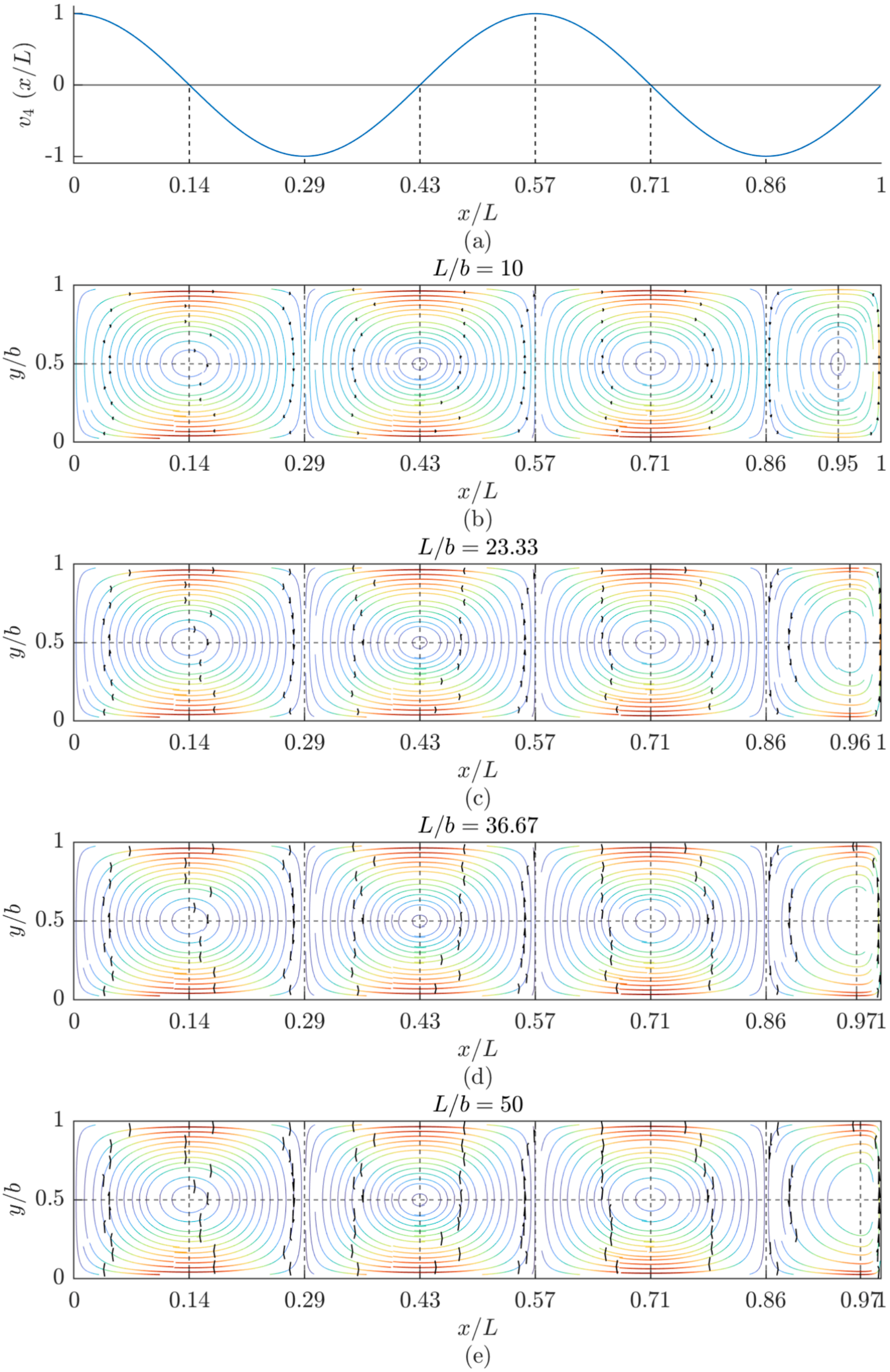

Fig. 14. Eddy current density maps for the fourth bending mode of the sliding-pinned reference beam: (a) modal velocity; (b) eddy current density map for $L/b = 10$; (c) eddy current density map for $L/b = 23.33$; (d) eddy current density map for $L/b = 36.67$ and (e) eddy current density map for $L/b = 50$.

aspect ratios, $L/b = 10,\ 23.33,\ 36.67$ and 50, at each mode. Eq. (4) has been validated in every case.

5.2. Analysis of the clamped-free and sliding-pinned reference beam

The modal velocities of the first four bending modes for the clamped-free and sliding-pinned reference beam, as described in Eq. (2), are applied, and the resulting eddy current density maps are shown in Figs. 7–14 for four evenly spaced ratios L/b, from 10 to 50. In all cases, the positions along the beam's length and width are expressed using the normalised coordinates x/L and y/b, respectively.

The first aspect to highlight regarding the eddy current maps is that the number of eddies generated corresponds to the mode number and are symmetric with respect to the longitudinal axis of the beam. Additionally, the eddies rotate anticlockwise when $\frac{\partial v(x)}{\partial x} > 0$ and clockwise when $\frac{\partial v(x)}{\partial x} < 0$. This can be demonstrated using the differential form of Eq. (11), which is derived by applying Stokes' theorem to both sides, resulting in

$$\nabla \times (\rho \boldsymbol{J}) = B\frac{\partial v(x)}{\partial x}\hat{\boldsymbol{z}} \tag{30}$$

The boundary between two consecutive eddies in the x-direction coincides with the points where the modal velocity reaches a local maximum or minimum. Since at the boundary of an eddy $\nabla \times (\rho \boldsymbol{J}) = \boldsymbol{0}$, this can only occur when $\frac{\partial v(x)}{\partial x} = 0$, corresponding to the points where the modal velocity reaches a local maximum or minimum.

The eddy exhibiting the highest values is located closest to the free end of the beam, with its maximum value found at the top and bottom edges of the beam width. In contrast, the eddy exhibiting the minimum values is positioned closest to the clamped end, regardless of the mode number.

The centres of the eddies are positioned where the modal velocity has zero curvature. An exception is found with the eddy closest to the free and pinned beam ends, where, as the length of the beam increases, the centre of the eddy shifts closer to those ends. This occurs because, for these boundary conditions, the curvature is zero at the beam ends. Since no eddy centre can be located precisely at the beam ends, as this would violate the charge conservation principle in Eq. (12), the system compensates by generating the eddy near the beam ends. As observed in the eddy current maps, as the beam length increases, the eddy progressively moves closer to the free and pinned ends across all modes, resulting in a non-symmetric eddy, unlike the others that remain symmetric.

It is concluded that, for each mode, the positions of the eddy centres and the boundaries between consecutive eddies along beam's longitudinal axis are independent of the beam length, except for the eddy closest to the free and pinned beam ends. For this eddy, its centre shifts closer to the ends as the beam length increases. These conclusions can be further corroborated by inspecting the eddy current maps provided in Appendix for these cases and the remaining boundary conditions.

6. Parametric study and design methodology

This Section introduces a methodology for designing beams with eddy current damping. The design variables include the beam geometry (length L, width b, and thickness d), material properties (Young's modulus E, volumetric density ρ_{v}, and electrical conductivity σ), the modal velocity magnitude $v_{\max}$, the magnetic field magnitude B, and the beam boundary conditions specified in Table 1. The output variables, considered for the first four bending modes, include electrical variables (the maximum eddy current density in the x- and y-directions, $J_{x,\max}$ and $J_{y,\max}$, respectively, the average dissipated power P, and the total current I), structural variables (the angular natural frequency ω and stiffness k), and the coefficients associated with the electromechanical model depicted in Fig. 2 (electrical resistance R and bar length ℓ), as well as the equivalent Kelvin-Voight mechanical model shown in Fig. 3 (viscous coefficient c and viscous damping ratio ζ).

The methodology begins by examining the equations to determine the influence of each design variable on the output variables. This analysis leads to the conclusion that straightforward relationships can be established for most design and output variables, except for beam length and boundary conditions. Consequently, a simple equation is proposed for each output variable applicable to any beam, based on the output variables of a reference beam with the same aspect ratio L/b, to facilitate the design of other beams. Subsequently, a parametric study is carried out to investigate the influence of the length-to-width ratio of a reference beam across the ten boundary conditions detailed in Table 1. This approach enables the output variables for any design beam to be derived from the reference beam output variables and the established relationships, significantly simplifying the design process for beams with eddy current damping. Finally, an example application is presented in the concluding subsection.

6.1. Influence of the design variables on the output variables

To establish a methodology for analysing beams with eddy current damping, the equations of each output variable are meticulously examined. First, from Eqs. (15), (17), and (18), it can be concluded that the current density fields are identical for beams with the same aspect ratio L/b. Consequently, the relationship between $J_x(x,y)$ for a beam and that of a reference beam with the same aspect ratio is given by

$$\frac{J_x(x,y)}{J_{x_0}(x,y)} = \frac{\sigma}{\sigma_0}\,\frac{v_{\max}}{v_{\max_0}}\,\frac{B}{B_0}, \tag{31}$$

where $(\bullet)_0$ denotes the variables of the reference beam. The same relationship applies between $J_y(x,y)$ and $J_{y_0}(x,y)$.

This result highlights the critical role of the beam's aspect ratio in determining the output variables, enabling the derivation of relationships that express these variables as functions of the aspect ratio from: Eq. (21) for the average dissipated power P; Eq. (23) for the total current I; Eq. (3) for the natural angular frequency ω; Eq. (24) for the stiffness k; Eq. (25) for the electrical resistance R; Eq. (26) for the bar length ℓ; Eq. (27) for the viscous coefficient c; and Eq. (29) for the viscous damping ratio ζ.

As an example, Eq. (21), referring to the dissipated power, can be rewritten as

$$P = \frac{dh_y^2}{\sigma}\frac{h_x}{h_y}\sum_{j=1}^{N}\frac{J_{x_r}^2\left(x_j,y_j\right) + J_{y_r}^2\left(x_j,y_j\right)}{2} \tag{32}$$

From this, it follows that the dissipated power of any beam relates to that of a reference beam with the same aspect ratio as

$$\frac{P}{P_0} = \left(\frac{b}{b_0}\right)\frac{d}{d_0}\frac{\sigma}{\sigma_0}\left(\frac{v_{\max}}{v_{\max_0}}\right)^2\left(\frac{B}{B_0}\right)^2 \tag{33}$$

After examining all the aforementioned equations, the effect of the design variables on the output variables is summarised in Table 3, where each α_m is the ratio of each design variable between the design beam and a reference beam with the same aspect ratio, for instance $\alpha_b = b/b_0$. It is important to note that Table 3 applies directly to all the different beam boundary conditions presented in Table 1 and is valid for any mode. For clarity, the following equation serves as an example for determining the viscous damping ratio of a design beam, ζ, when the viscous damping ratio of the reference beam, ζ_0, is known:

$$\zeta = \alpha_b^2\alpha_d^{-1}\alpha_E^{-1/2}\alpha_{\rho_v}^{-1/2}\alpha_\sigma\alpha_B^2\zeta_0 \tag{34}$$

The variations of each output variable relative to the reference beam can be determined by multiplying all the individual values of a row for each studied output variable, as demonstrated in Eq. (34). Thus, Table 3 highlights which output variables have the greatest influence on the mechanical behaviour of the beam. For example, if the aim of a particular application is to increase the beam's dissipated power and viscous damping ratio, an effective approach would be to use a wider beam or to increase the magnitude of the external magnetic field. However, if the goal is to increase the electrical resistance, altering the beam's width and the magnitude of the external magnetic field would have no effect. Instead, reducing the beam's thickness is one way to achieve this, although this would come at the cost of reducing the dissipated power in the beam.

6.2. *Influence of the beam length on the output variables*

Since no straightforward relationship is readily identified for the beam length, in contrast to the other design variables, a study is conducted on a reference beam for the ten boundary conditions listed in Table 1. This study involves varying the reference beam length L from a minimum aspect ratio of $L/b = 10$ to a maximum of 50, using 1000 linearly spaced samples. The geometry and material properties of the reference beam are outlined in Table 2, while the boundary conditions are detailed in Table 1. The results for the previously described output variables are illustrated in Figs. 15-24.

The following presents an analysis of the trends observed in Figs. 15-24.

- The maximum values of the eddy current density maps in the x- and y-directions increase with the mode number. These values decrease as the beam length increases, with the rate of decrease being greater for higher modes. For longer beams, referring to those with an aspect ratio of 40 or more, $J_{x,\max}$ decreases proportionally to $(L/b)^{-1}$, whereas $J_{y,\max}$ decreases proportionally to $(L/b)^{-2}$ for each mode.

Table 3
Relationships between the output variables of the design beam and those of a reference beam with the same aspect ratio.

Ratio	b	d	E	ρ_v	σ	$v_{\max}$	B
$J_{x,\max}/J_{x,\max_0}$	1	1	1	1	α_σ	α_v	α_B
$J_{y,\max}/J_{y,\max_0}$	1	1	1	1	α_σ	α_v	α_B
P/P_0	α_b^2	α_d	1	1	α_σ	α_v^2	α_B^2
I/I_0	α_b	α_d	1	1	α_σ	α_v	α_B
ω/ω_0	α_b^{-2}	α_d	$\alpha_E^{1/2}$	$\alpha_{\rho_v}^{-1/2}$	1	1	1
k/k_0	α_b^{-2}	α_d^3	α_E	1	1	1	1
R/R_0	1	α_d^{-1}	1	1	α_σ^{-1}	1	1
ℓ/ℓ_0	α_b	1	1	1	1	1	1
c/c_0	α_b^2	α_d	1	1	α_σ	1	α_B^2
ζ/ζ_0	α_b^2	α_d^{-1}	$\alpha_E^{-1/2}$	$\alpha_{\rho_v}^{-1/2}$	α_σ	1	α_B^2

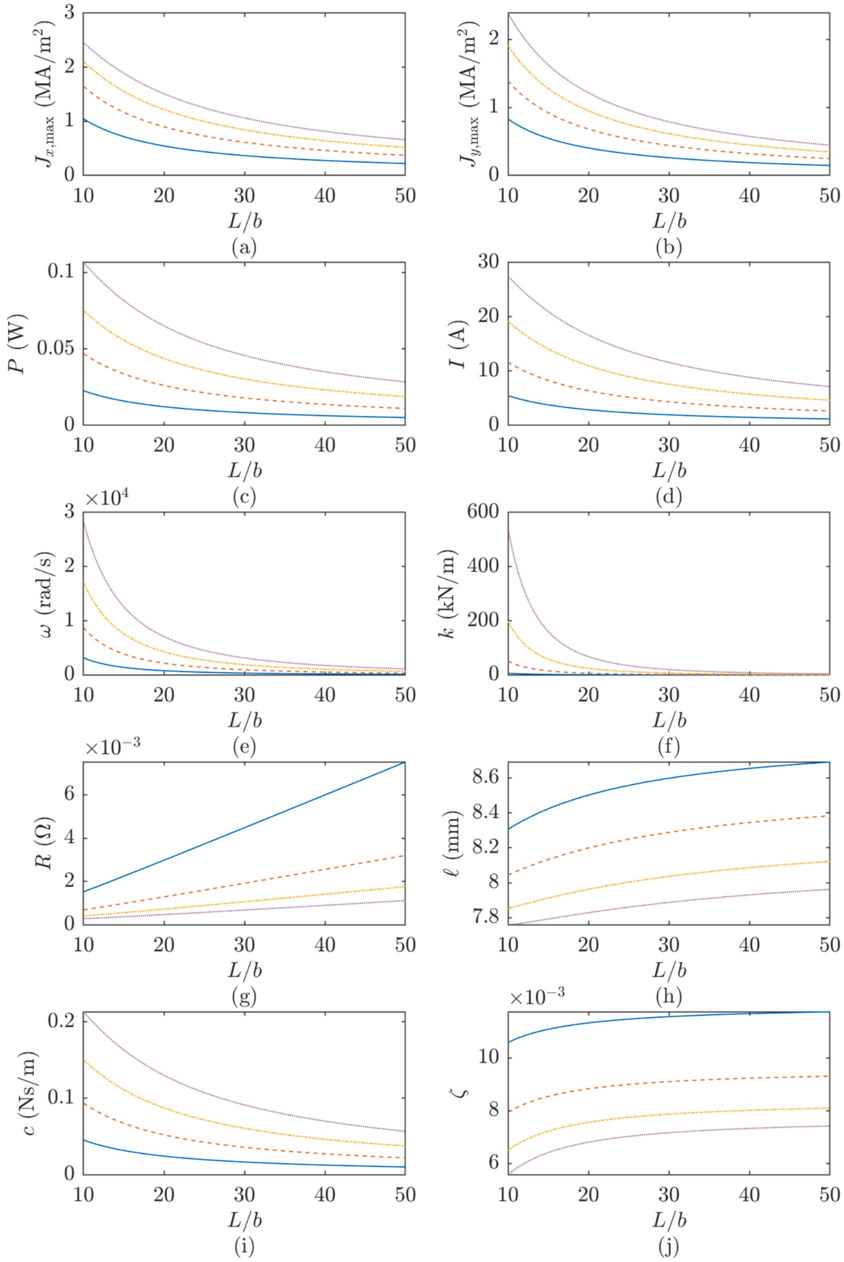

Fig. 15. Output variables for the free-free reference beam across modes 1 (——), 2 (– – –), 3 (– · –), and 4 (·······): (a) maximum eddy current density in the x-direction; (b) maximum eddy current density in the y-direction; (c) average dissipated power; (d) total current; (e) angular natural frequency; (f) stiffness; (g) electrical resistance; (h) bar length; (i) viscous coefficient and (j) viscous damping ratio.

- The average dissipated power P is greater for shorter beams across all modes and boundary conditions, exhibiting a decreasing trend as beam length increases. For longer beams, P is proportional to $(L/b)^{-1}$ for each mode, indicating that shorter beams result in greater dissipation of mechanical energy. Additionally, the dissipated power increases with the mode number.
- The total current circulating in the beam I decreases with beam length for all modes and boundary conditions. However, the total current increases with the mode number. For longer beams, I is proportional to $(L/b)^{-1}$ for each mode.
- The angular natural frequency ω decreases proportionally to $(L/b)^{-2}$ as the beam length increases for all modes and boundary conditions, as expected from Eq. (3). As the mode number increases, the angular natural frequency also rises, corresponding to an increase in the eigenvalue λ.

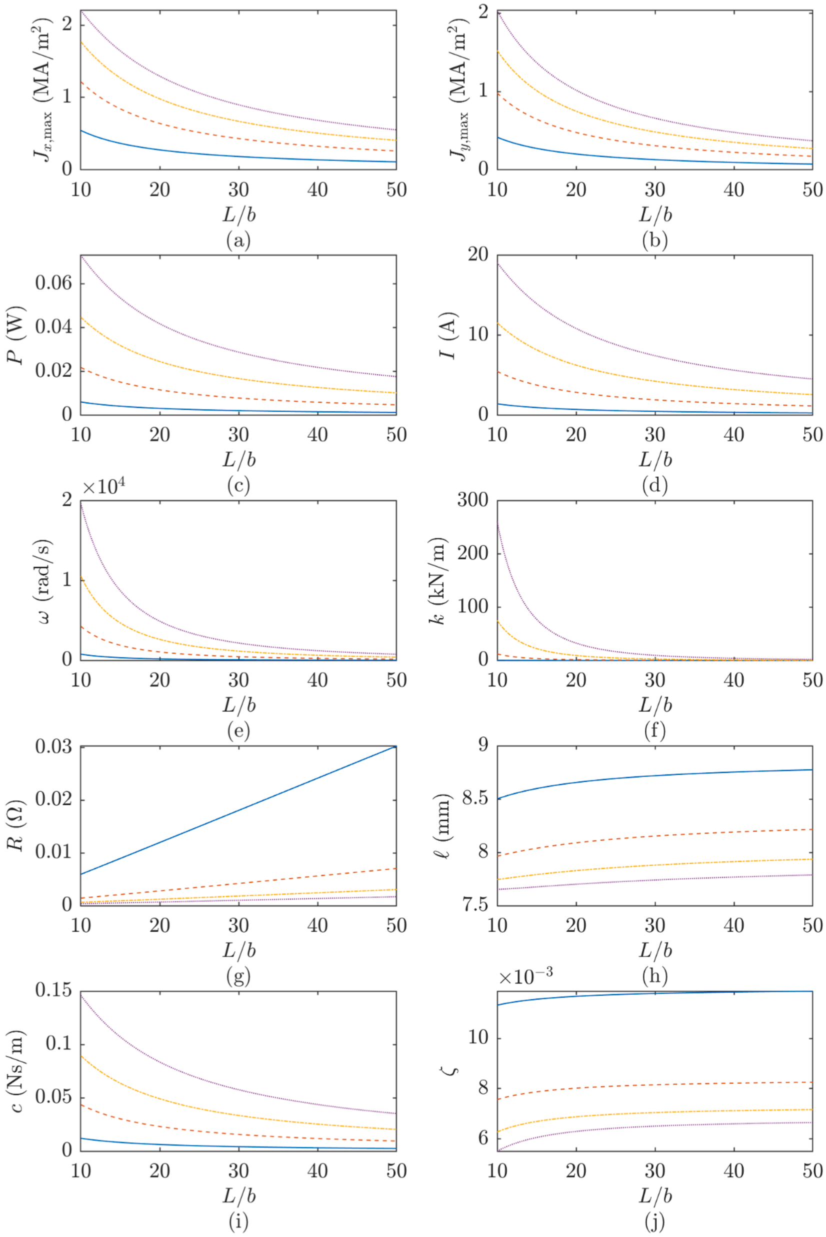

Fig. 16. Output variables for the free-sliding reference beam across modes 1 (—), 2 (– – –), 3 (– · –), and 4 (·······): (a) maximum eddy current density in the x-direction; (b) maximum eddy current density in the y-direction; (c) average dissipated power; (d) total current; (e) angular natural frequency; (f) stiffness; (g) electrical resistance; (h) bar length; (i) viscous coefficient and (j) viscous damping ratio.

- The stiffness k decreases proportionally to $(L/b)^{-3}$ for all modes and boundary conditions, in agreement with Eq. (24). Since the stiffness depends on the angular frequency and the modal mass, the stiffness k also increases as the mode number rises.
- The electrical resistance R increases linearly with the aspect ratio L/b across all modes and boundary conditions. As the mode number increases, the electrical resistance decreases. This aligns with observations for maximum currents and dissipated powers, as higher electrical resistance causes more rapid current decay, resulting in reduced power dissipation.
- The bar length ℓ generally increases as the mode number increases, except in the free-free and free-sliding beams, where the opposite behaviour occurs. A notable phenomenon is observed in the clamped-free beam, where the length ℓ is greater for mode 2 than for the other modes, due to the hyperbolic terms of the applied velocity field. Regarding the trend of ℓ as the ratio L/b increases, it is observed that in the free-free, free-sliding, and clamped-free beams, ℓ increases slightly with the ratio across all modes. For the sliding-sliding beam, a decay is noted, and as the ratio increases further, the length ℓ tends to converge to the same value for all modes. In the remaining beams, a slight increase in ℓ is observed for beams with a ratio L/b below 20 in mode 1, contrary to the

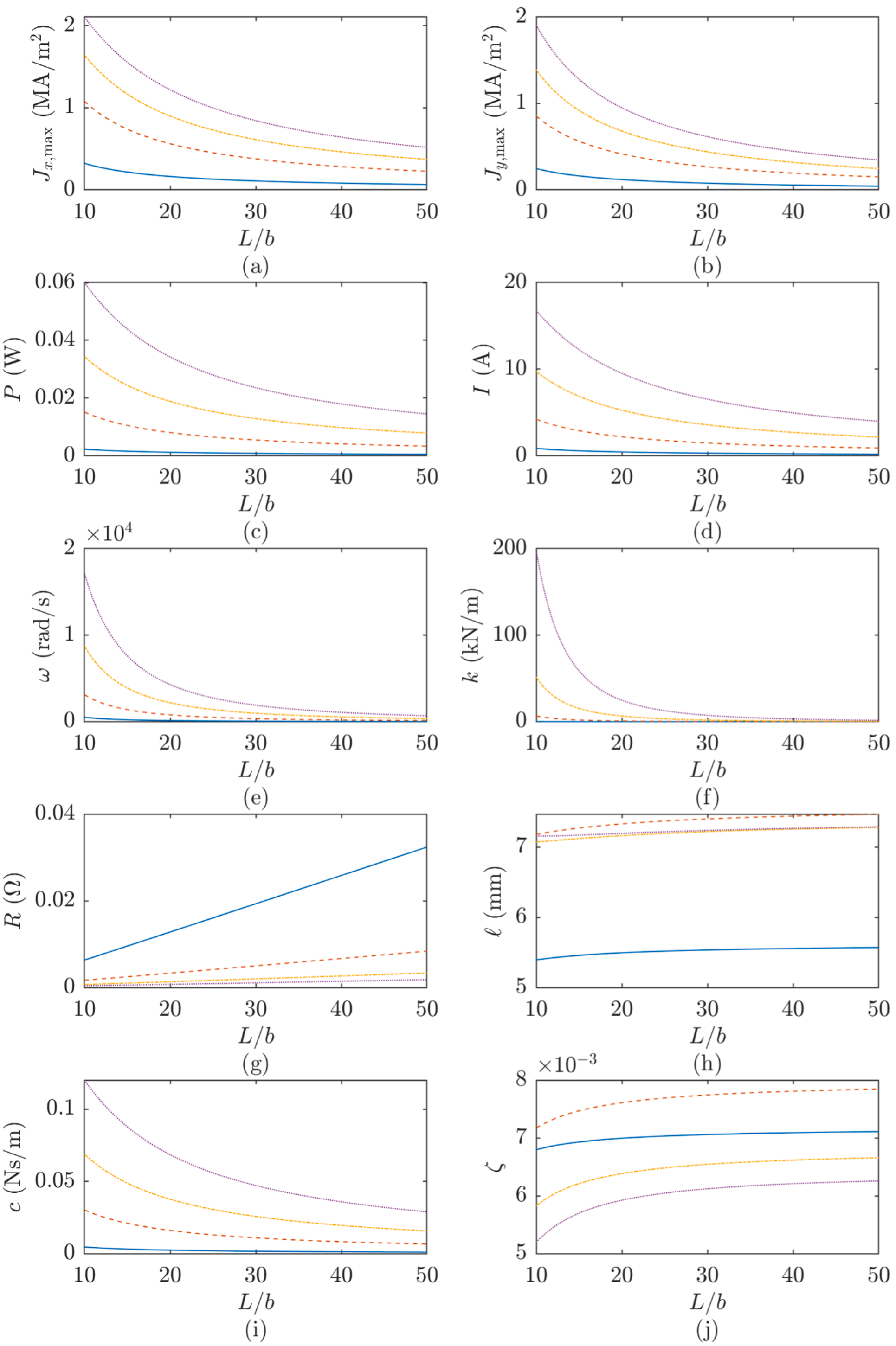

Fig. 17. Output variables for the clamped-free reference beam across modes 1 (—), 2 (– – –), 3 (– · –), and 4 (·······): (a) maximum eddy current density in the x-direction; (b) maximum eddy current density in the y-direction; (c) average dissipated power; (d) total current; (e) angular natural frequency; (f) stiffness; (g) electrical resistance; (h) bar length; (i) viscous coefficient and (j) viscous damping ratio.

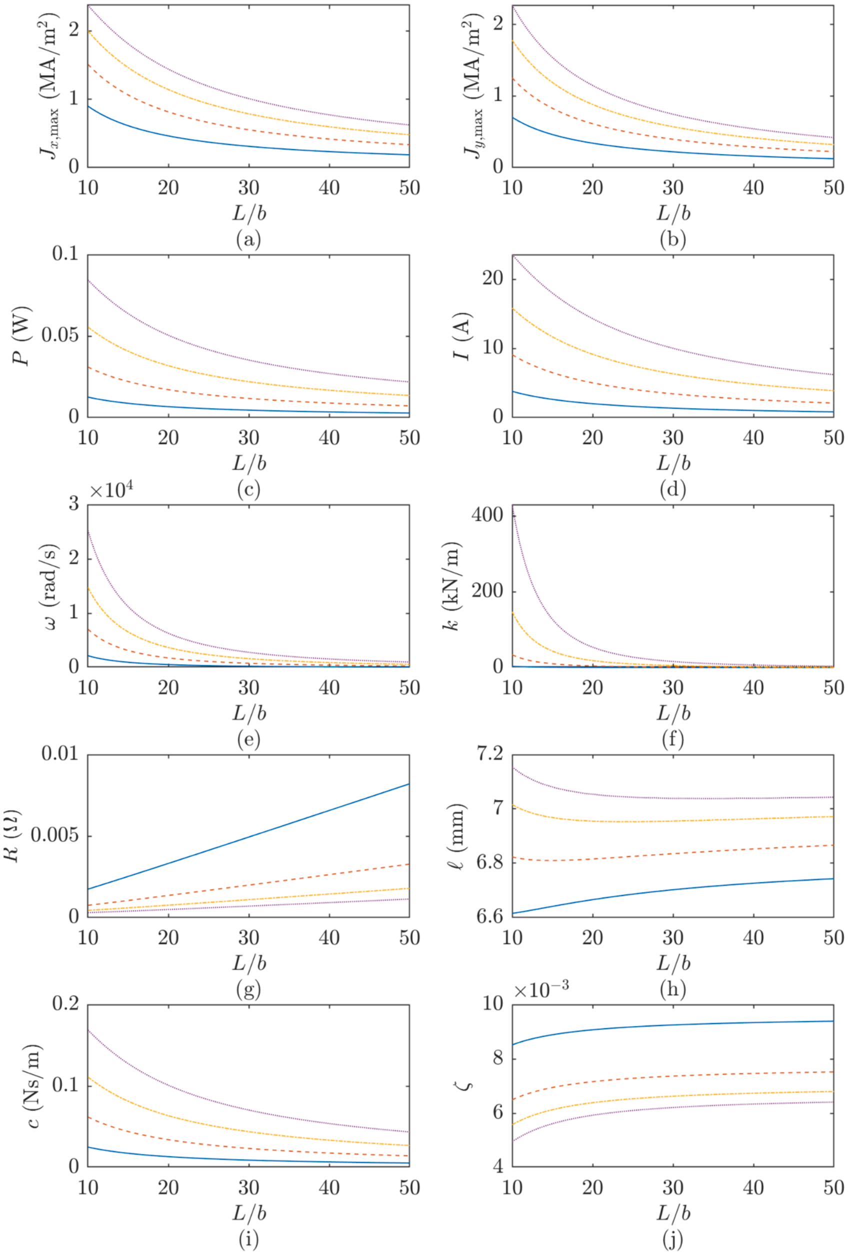

Fig. 18. Output variables for the free-pinned reference beam across modes 1 (——), 2 (– – –), 3 (– · –), and 4 (·······): (a) maximum eddy current density in the x-direction; (b) maximum eddy current density in the y-direction; (c) average dissipated power; (d) total current; (e) angular natural frequency; (f) stiffness; (g) electrical resistance; (h) bar length; (i) viscous coefficient and (j) viscous damping ratio.

other modes, where a slight decrease in ℓ is observed. As the ratio L/b exceeds 20, ℓ tends to remain constant across all modes. As indicated in Section 3, ℓ represents the equivalent length of the conductor, which is directly related to the shape of the current lines. The shape of these current lines is highly dependent on the boundary conditions and the mode, as can be seen in Section 5 and the Appendix. This makes ℓ particularly sensitive to these factors in comparison to the other output variables.

- The damping coefficient c decreases as the beam length increases for any mode and boundary condition. As the mode number increases, the value of the damping coefficient also increases. These results are consistent with the behaviour of the induced currents. For longer beams, c decreases proportionally to $(L/b)^{-1}$.
- The viscous damping ratio ζ is generally higher for shorter beams and reaches a constant value for each mode beyond a ratio L/b of 30. This output variable is also observed to be the most sensitive one to boundary conditions. As the mode number increases, the viscous damping ratio decreases, with the most significant reduction occurring from mode 1 to mode 2. An exception to this trend is

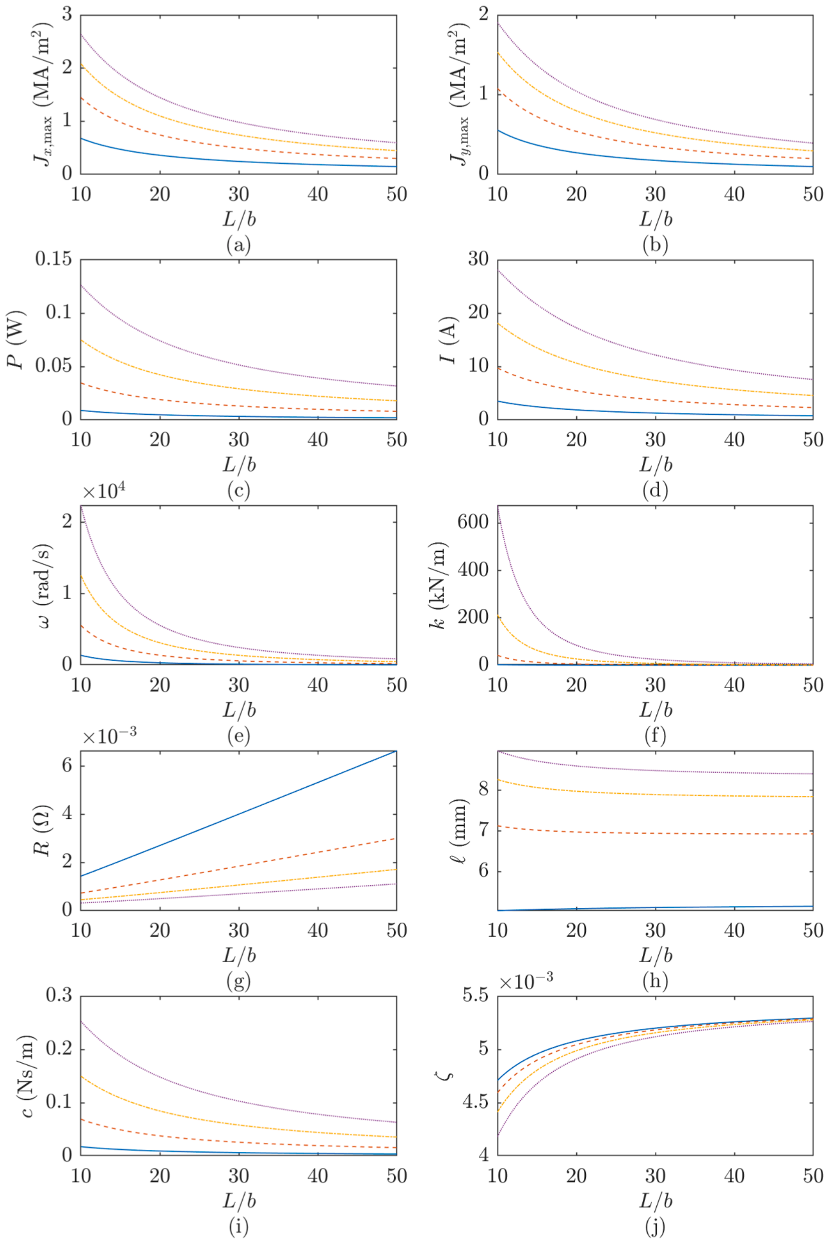

Fig. 19. Output variables for the pinned–pinned reference beam across modes 1 (—), 2 (– –), 3 (–·–), and 4 (⋯): (a) maximum eddy current density in the x-direction; (b) maximum eddy current density in the y-direction; (c) average dissipated power; (d) total current; (e) angular natural frequency; (f) stiffness; (g) electrical resistance; (h) bar length; (i) viscous coefficient and (j) viscous damping ratio.

observed in beams with clamped boundary conditions. For the clamped-free beam, the viscous damping ratio increases from mode 1 to mode 2 and then decreases. In clamped-pinned, clamped–clamped, and clamped-sliding beams, the viscous damping ratio of mode 4 is not higher than the other modes in shorter beams. This behaviour is attributed to the hyperbolic terms of the applied velocity field in these cases.

6.3. *Application example*

A practical example is provided for a beam with eddy current damping under clamped-free boundary conditions, utilising the output variables presented in Fig. 17 and the relationships detailed in Table 3. The design variables (beam geometry, material properties, modal velocity magnitude, and magnetic field magnitude) for the design beam in this example are summarised in Table 4, alongside each ratio α_m.

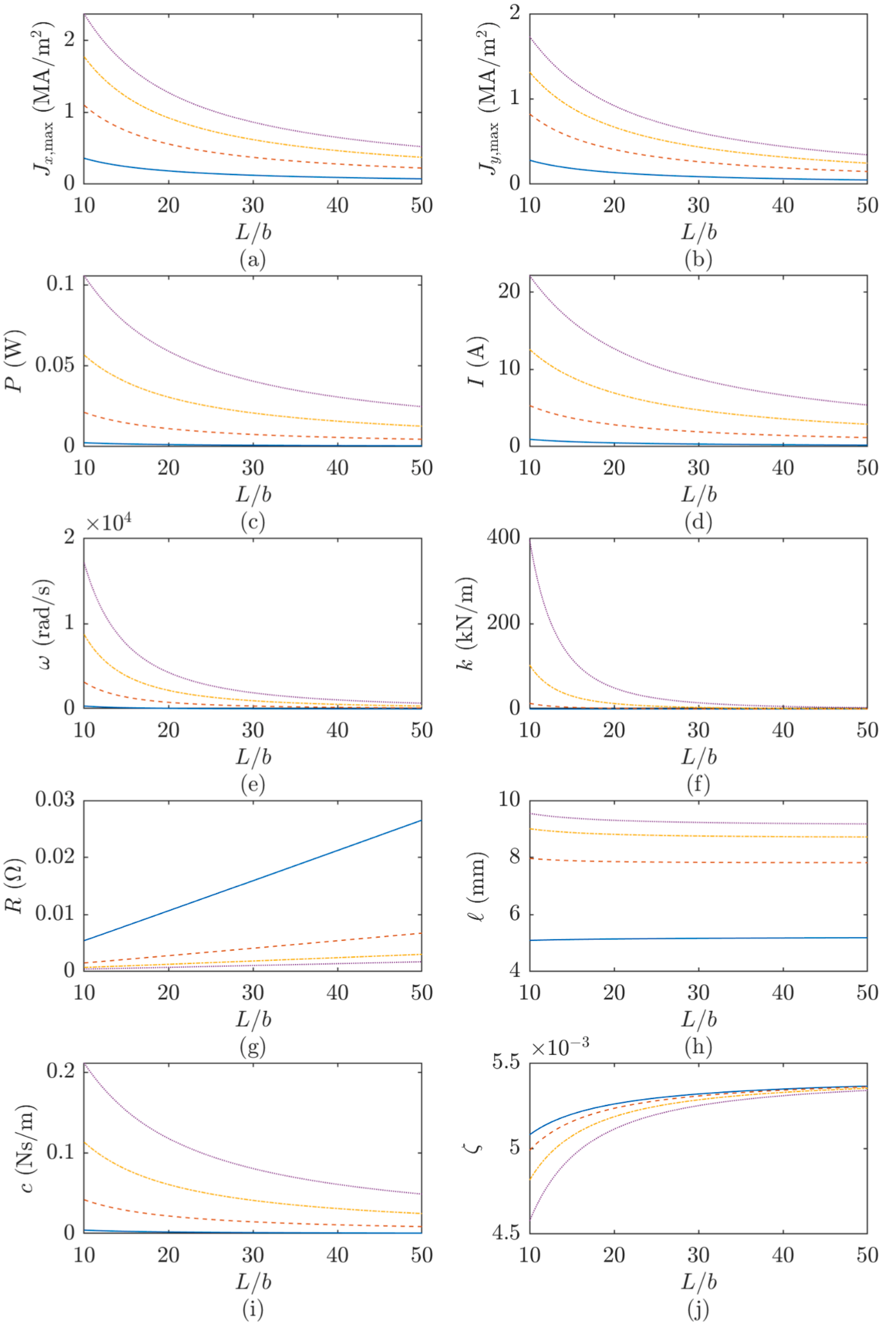

Fig. 20. Output variables for the sliding-pinned reference beam across modes 1 (—), 2 (– – –), 3 (– · –), and 4 (·····): (a) maximum eddy current density in the x-direction; (b) maximum eddy current density in the y-direction; (c) average dissipated power; (d) total current; (e) angular natural frequency; (f) stiffness; (g) electrical resistance; (h) bar length; (i) viscous coefficient and (j) viscous damping ratio.

The values provided in Table 4, together with the relationships in Table 3 and the output variables from Fig. 17 for $L/b = 30$, are employed to calculate the output variables for the clamped-free design beam in this example for any mode. As an illustration, Table 5 presents the output variables for both the reference beam and the design beam in this example for the third mode.

The procedure utilised to obtain the output variables in this example is applicable to all ten boundary conditions and for any mode. This methodology facilitates the determination of the damping behaviour of beams with eddy current damping without the need to solve the eddy currents explicitly. This capability is particularly valuable in design applications where vibrations are attenuated through eddy currents.

Furthermore, a MATLAB application has been developed based on the proposed methodology, and it is included as supplementary

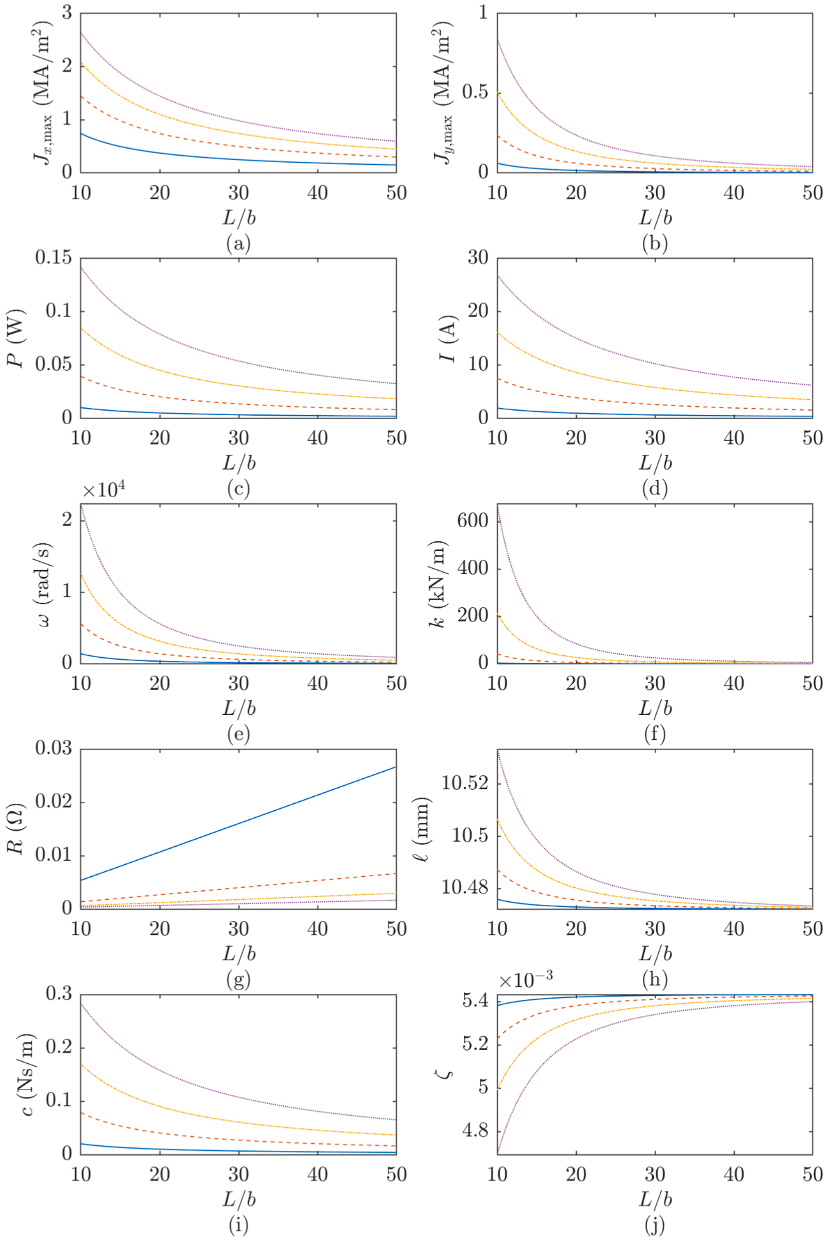

Fig. 21. Output variables for the sliding-sliding reference beam across modes 1 (——), 2 (– – –), 3 (–·–), and 4 (·····): (a) maximum eddy current density in the x-direction; (b) maximum eddy current density in the y-direction; (c) average dissipated power; (d) total current; (e) angular natural frequency; (f) stiffness; (g) electrical resistance; (h) bar length; (i) viscous coefficient and (j) viscous damping ratio.

material.

For illustrative purposes, a design flowchart outlining the steps to apply the proposed methodology is shown in Fig. 25.

7. Conclusions

This study presents a methodology for designing beams with eddy current damping, specifically developed for engineering applications focused on vibration attenuation. The methodology centres in thin metallic non-magnetic beams that vibrate in the presence of an external, static, and uniform magnetic field, with self-inductance effects neglected. The beam's vibration is characterised by bending mode shapes, and different combinations of beam boundary conditions are considered.

The methodology involves numerically solving the eddy current problem for a reference beam with varying lengths and ten different boundary conditions, creating a comprehensive database of results. This database is then used to determine the output

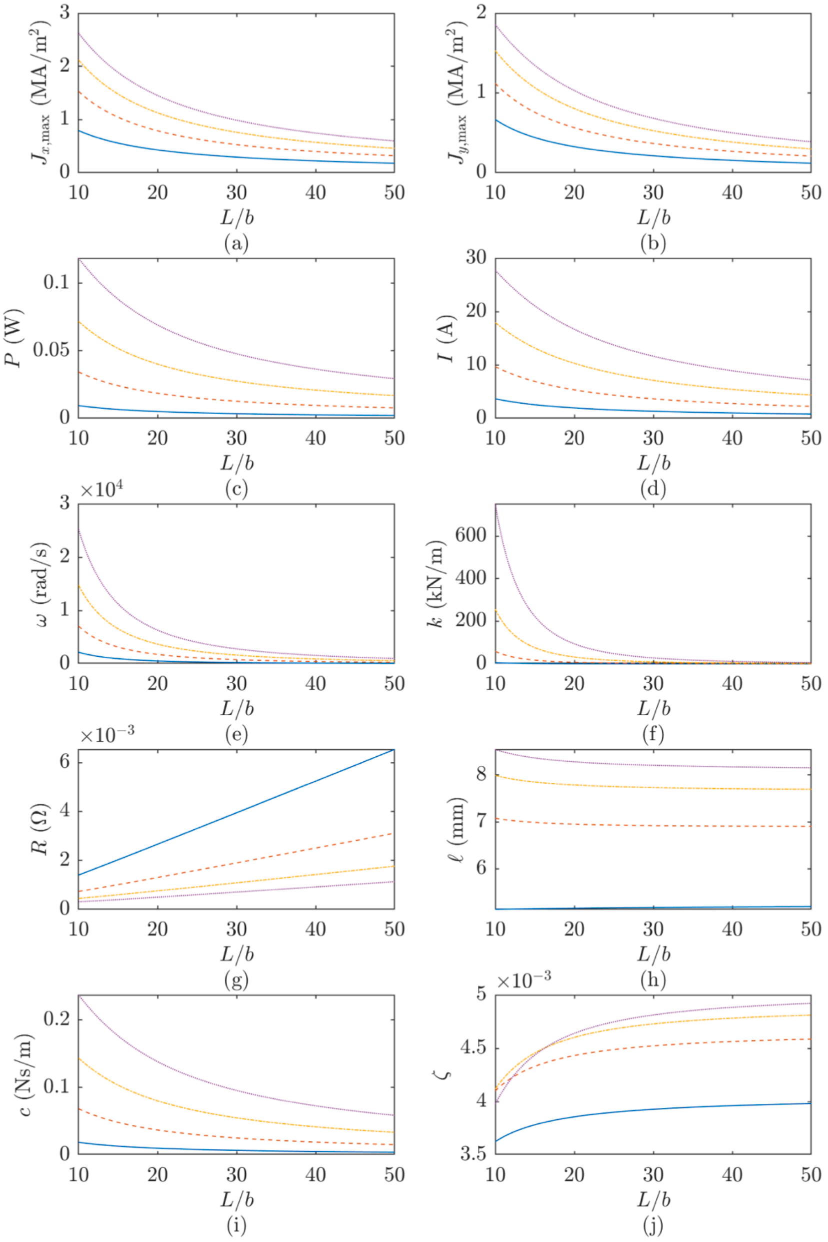

Fig. 22. Output variables for the clamped-pinned reference beam across modes 1 (—), 2 (– – –), 3 (– · –), and 4 (⋯): (a) maximum eddy current density in the x-direction; (b) maximum eddy current density in the y-direction; (c) average dissipated power; (d) total current; (e) angular natural frequency; (f) stiffness; (g) electrical resistance; (h) bar length; (i) viscous coefficient and (j) viscous damping ratio.

variables of other beams based on their design variables. The design variables in this study include the beam geometry, material properties, velocity magnitude, magnetic field magnitude, and boundary conditions. The output variables, which allow for the prediction of the beam's mechanical behaviour, include electrical variables, structural variables, and coefficients associated with two simplified equivalent models of the beam: an electromechanical model and the mechanical Kelvin-Voight model.

After solving the eddy current problem for the reference beam, simple equations have been derived to obtain the output variables of any design beam directly from the reference beam's output variables. This approach avoids the need to solve the complex eddy current problem for each design beam individually, significantly simplifying the numerical procedures and, as a result, the design process for beams with eddy current damping.

Furthermore, the eddy current maps for the reference beam have been analysed, revealing that the different types of beam boundary conditions directly affect the distribution of eddies across the beam surface. It has been deduced that the boundary between two consecutive eddies along the beam's longitudinal axis is independent of beam length for each mode and across all boundary

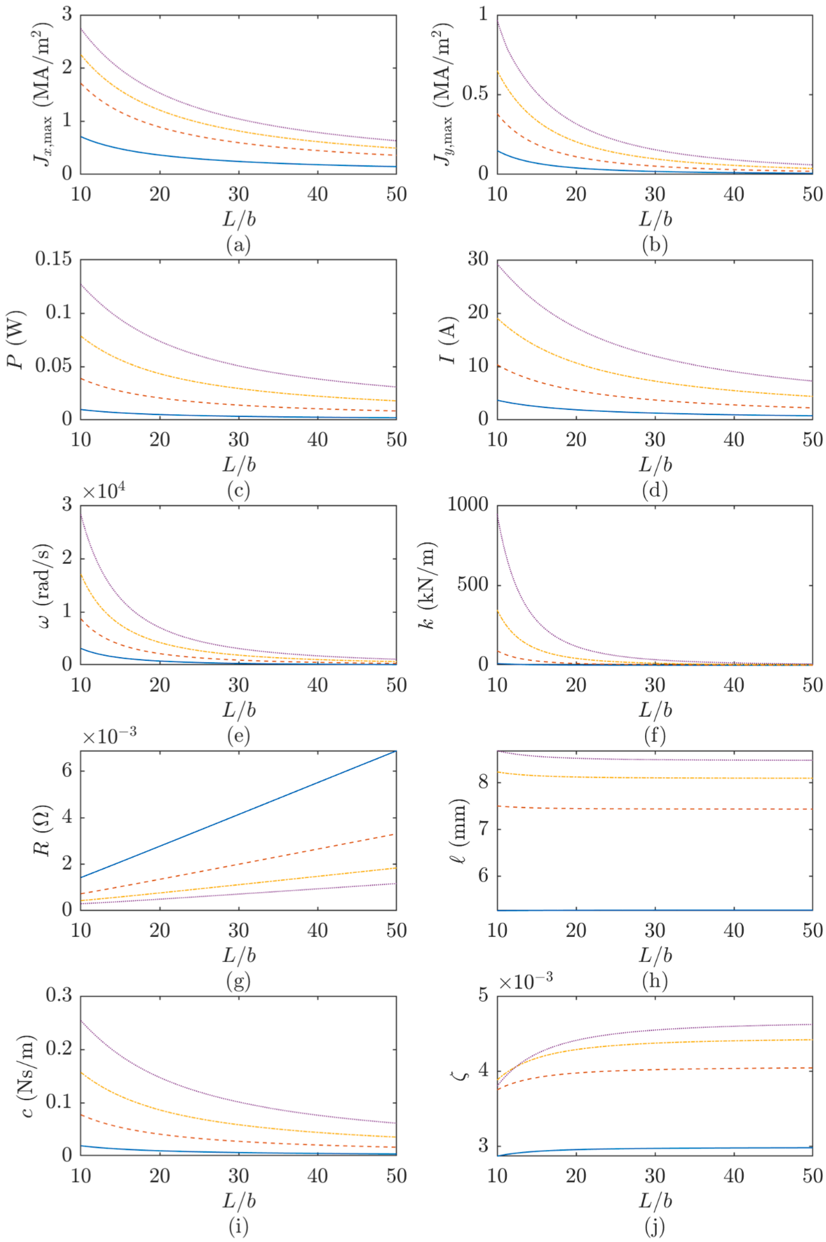

Fig. 23. Output variables for the clamped–clamped reference beam across modes 1 (━━), 2 (– – –), 3 (- · -), and 4 (·····): (a) maximum eddy current density in the x-direction; (b) maximum eddy current density in the y-direction; (c) average dissipated power; (d) total current; (e) angular natural frequency; (f) stiffness; (g) electrical resistance; (h) bar length; (i) viscous coefficient and (j) viscous damping ratio.

conditions. The positions of the eddy centres along the beam's longitudinal axis are also independent of beam length for all modes, except for the eddy centre closest to a free or pinned end. In these cases, it is observed that the centre shifts closer to these beam ends as the beam length increases.

In conclusion, the work presented in this paper offers a valuable resource for designing beams with eddy current damping. This resource is beneficial both qualitatively, as it enhances understanding of the nature of induced eddy currents, and quantitatively, as it provides a methodology for analysing the output variables and simplifying numerical procedures. Additionally, the MATLAB application developed as part of this work, which is included as supplementary material, serves as a practical and useful tool for designers of beams with eddy current damping.

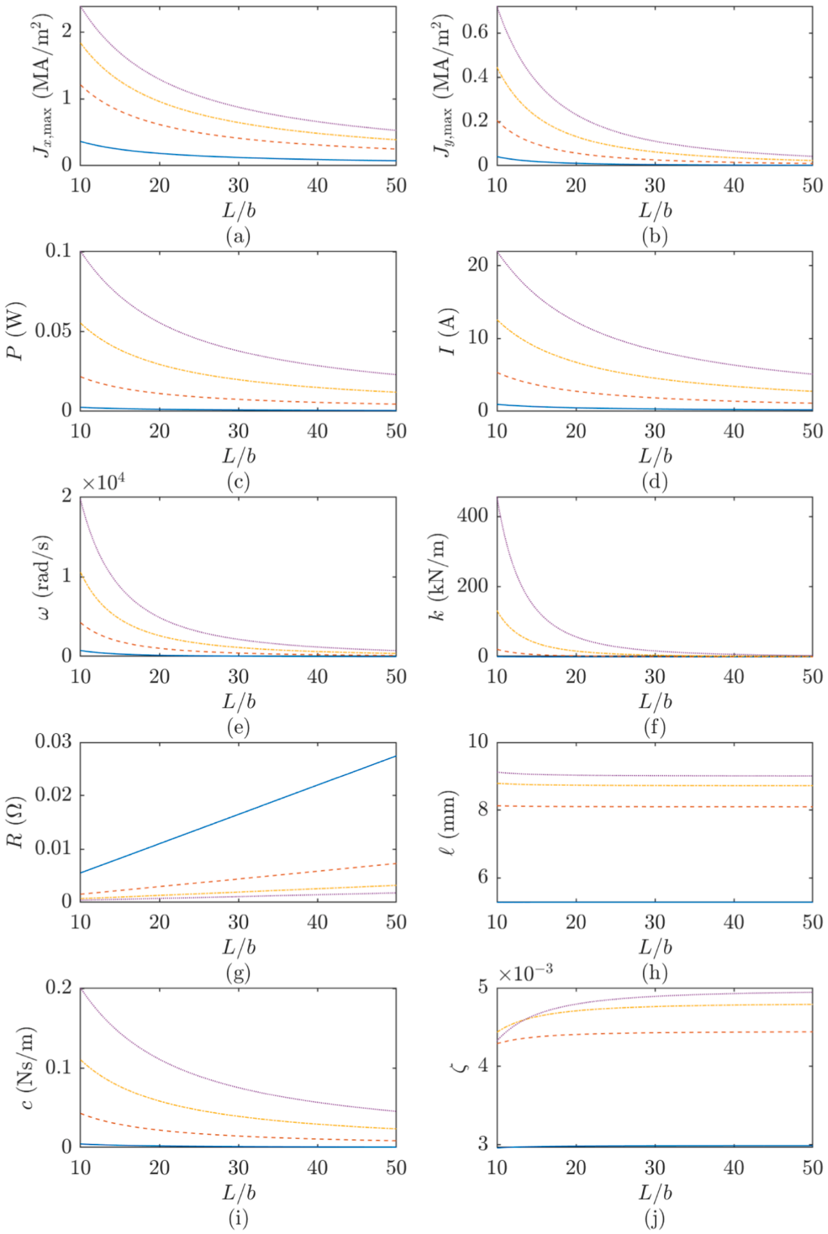

Fig. 24. Output variables for the clamped-sliding reference beam across modes 1 (—), 2 (– – –), 3 (– · –), and 4 (⋯⋯): (a) maximum eddy current density in the x-direction; (b) maximum eddy current density in the y-direction; (c) average dissipated power; (d) total current; (e) angular natural frequency; (f) stiffness; (g) electrical resistance; (h) bar length; (i) viscous coefficient and (j) viscous damping ratio.

Table 4
Design variables and ratios for the clamped-free design beam of the example.

Property	Value	Ratio	Value
L (mm)	600	–	–
b (mm)	20	α_b	2
d (mm)	0.8	α_d	0.8
E (GPa)	68.25	α_E	1.05
ρ_v (kg/m^3)	3915	α_{ρ_v}	1.45
σ (MS/m)	7	α_σ	1.4
$v_{\max}$ (m/s)	0.9	α_v	0.9
B (T)	0.8	α_B	0.8

Table 5
Output variables for the clamped-free reference beam and the design beam of the example (third mode).

Result	Reference beam	Design beam
$J_{x,\max}$ (MA/m^2)	0.611	0.616
$J_{y,\max}$ (MA/m^2)	0.439	0.443
P (mW)	12.9	29.88
I (A)	3.56	5.75
ω (rad/s)	971.0	165.0
k (kN/m)	1.91	0.257
R (mΩ)	2.02	1.81
ℓ (mm)	7.22	14.4
c (mNs/m)	25.7	73.8
ζ (-)	6.54×10^{-3}	23.8×10^{-3}

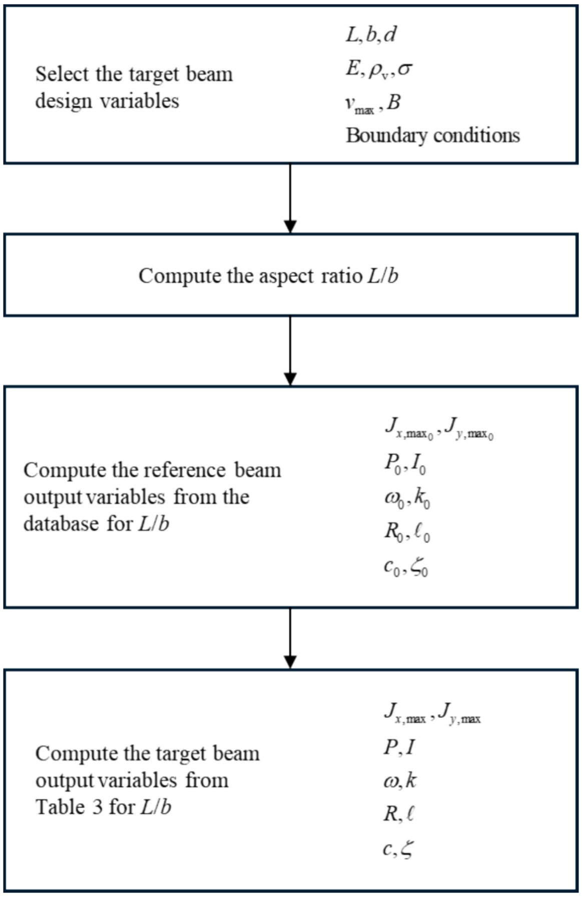

Fig. 25. Design process flowchart.

Declaration of Generative AI and AI-assisted technologies in the writing process

During the preparation of this work the authors used ChatGPT in order to improve the language and readability of their paper. After using this tool, the authors reviewed and edited the content as needed and take full responsibility for the content of the publication.

CRediT authorship contribution statement

Mikel Brun: Writing – original draft, Software, Methodology, Formal analysis, Conceptualization. **Fernando Cortés:** Writing – review & editing, Supervision, Methodology, Formal analysis, Conceptualization. **María Jesús Elejabarrieta:** Writing – review & editing, Supervision, Methodology, Formal analysis, Conceptualization.

Declaration of competing interest

The authors declare that they have no known competing financial interests or personal relationships that could have appeared to influence the work reported in this paper.

Acknowledgements

This study has received financial support from the Department of Education of the Basque Government with the Research Group program IT1507-22.

Appendix A. Supplementary data

Supplementary data to this article can be found online at https://doi.org/10.1016/j.ymssp.2025.112790.

Data availability

All the results published in this paper were achieved using the data presented herein and may be reproduced in the same manner.

References

[1] B.M. Notaroš, Electromagnetics, International edition, Pearson, Upper Saddle River, NJ, 2011.
[2] M. Amjadian, A.K. Agrawal, A passive electromagnetic eddy current friction damper (PEMECFD): Theoretical and analytical modeling, Struct. Control Health Monit. 24 (2017) e1978.
[3] L. Ye, C. Liang, Y. Liu, D. Li, Z. Liu, Performance analysis and test of a novel eddy-current braking & heating system for electric bus, Energy Convers. Manag. 183 (2019) 440–449, https://doi.org/10.1016/j.enconman.2019.01.010.
[4] L. Liang, Z. Feng, Z. Chen, Seismic control of SDOF systems with nonlinear eddy current dampers, Appl. Sci. 9 (2019) 3427, https://doi.org/10.3390/APP9163427.
[5] B.B. Shobhana, V.R. Panchal, V.A. Matsagar, Research developments of eddy current dampers for seismic vibration control of structures, J. Vib. Eng. Technol. 12 (2024) 5953–5971, https://doi.org/10.1007/s42417-023-01229-4.
[6] H.A. Sodano, D.J. Inman, Non-contact vibration control system employing an active eddy current damper, J. Sound Vib. 305 (2007) 596–613, https://doi.org/10.1016/j.jsv.2007.04.050.
[7] E. Diez-Jimenez, R. Rizzo, M.-J. Gómez-García, E. Corral-Abad, Review of passive electromagnetic devices for vibration damping and isolation, Shock Vib. 2019 (2019) 1250707, https://doi.org/10.1155/2019/1250707.
[8] Z. Wang, Z. Cheng, G. Yin, W. Shen, A magnetic negative stiffness eddy-current inertial mass damper for cable vibration mitigation, Mech. Syst Signal Process. 188 (2023) 110013, https://doi.org/10.1016/j.ymssp.2022.110013.
[9] B. Ebrahimi, M.B. Khamesee, M.F. Golnaraghi, Design and modeling of a magnetic shock absorber based on eddy current damping effect, J. Sound Vib. 315 (2008) 875–889, https://doi.org/10.1016/j.jsv.2008.02.022.
[10] Z. Cheng, K. Bi, Z. Wang, R. Ma, W. Lin, Performance enhanced magnetic negative stiffness eddy-current damper: Numerical simulation and experimental investigation, Mech. Syst Signal Process. 223 (2025) 111890, https://doi.org/10.1016/j.ymssp.2024.111890.
[11] Z. Wang, Z. Chen, J. Wang, Feasibility study of a large-scale tuned mass damper with eddy current damping mechanism, Earthq. Eng. Eng. Vib. 11 (2012) 391–401, https://doi.org/10.1007/s11803-012-0129-x.
[12] L. Zuo, X. Chen, S. Nayfeh, Design and analysis of a new type of electromagnetic damper with increased energy density, J. Vib. Acoust. 133 (2011), https://doi.org/10.1115/1.4003407.
[13] L. Irazu, M.J. Elejabarrieta, A novel hybrid sandwich structure: Viscoelastic and eddy current damping, Mater. Des. 140 (2018) 460–472, https://doi.org/10.1016/j.matdes.2017.11.070.
[14] J. Yu, Design and optimization of wing structure for a fixed-wing unmanned aerial vehicle (UAV), Mod. Mech. Eng. 8 (2018) 249–263, https://doi.org/10.4236/mme.2018.84017.
[15] S. Kowalski, K. Opoka, J. Ciuła, Analysis of the end-of-life the front suspension beam of a vehicle, Eksploat. Niezawodn. 24 (2022) 446–454, https://doi.org/10.17531/ein.2022.3.6.
[16] H.A. Sodano, J.-S. Bae, D.J. Inman, W. Keith Belvin, Concept and model of eddy current damper for vibration suppression of a beam, J. Sound Vib. 288 (2005) 1177–1196, https://doi.org/10.1016/j.jsv.2005.01.016.
[17] G.J. Stein, P. Tobolka, R. Chmúrny, Ferromagnetic eddy current damper of beam transversal vibrations, J. Vib. Control 24 (2018) 892–903, https://doi.org/10.1177/1077546316654791.
[18] M. Brun, F. Cortés, M.J. Elejabarrieta, Numerical analysis of energy dissipation due to eddy currents in a vibrating beam, J. Sound Vib. 595 (2025) 118787, https://doi.org/10.1016/j.jsv.2024.118787.
[19] F. Cortés, O. Zarraga, I. Sarría, M.J. Elejabarrieta, Eddy currents damping understood as Zener viscoelastic damping, J. Sound Vib. 547 (2023) 117539, https://doi.org/10.1016/j.jsv.2022.117539.
[20] L. Irazu, M.J. Elejabarrieta, Analysis and numerical modelling of eddy current damper for vibration problems, J. Sound Vib. 426 (2018) 75–89, https://doi.org/10.1016/j.jsv.2018.03.033.
[21] Z. Shi, C.N. Loong, J. Shan, Equivalent circuit model of eddy current damping regarding frequency-dependence with test validation, Adv. Struct. Eng. 25 (2022) 188–200, https://doi.org/10.1177/13694332211050989.
[22] R.D. Blevins, Formulas for natural frequency and mode shape, Repr., reissue 1995 with minor corr, Krieger Publishing Company, Malabar, Florida, 1995, p. 1995.
[23] N.J. Siakavellas, Analytical modelling of eddy currents induced by a time-varying magnetic field in a conductive plate, COMPEL - Int, J. Comput. Math. Electr. Electron. Eng. 13 (1994) 497–508, https://doi.org/10.1108/eb010131.
[24] J. Nagel, Fast finite-difference calculation of eddy currents in thin metal sheets, Appl. Comput. Electromagn. Soc. J. 33 (2018) 575–584.
[25] D.J. Griffiths, Introduction to electrodynamics, 4th ed., Pearson, Boston, 2013.

[26] J.R. Nagel, Finite-difference simulation of eddy currents in nonmagnetic sheets via electric vector potential, IEEE Trans. Magn. 55 (2019) 1–8, https://doi.org/10.1109/TMAG.2019.2940204.

[27] J.R. Nagel, Numerical solutions to poisson equations using the finite-difference method, IEEE Antennas Propag. Mag. 56 (2014) 209–224, https://doi.org/10.1109/MAP.2014.6931698.

[28] L.D. Landau, E.M. Lifshit͡s, The current density and the conductivity, in: Electrodynamics of Continuous Media, 2nd ed., rev.enl, Pergamon, Oxford [Oxfordshire]; New York, 1984, pp. 86–90.